Event Detection in Spatio-Temporal Data Using Singular Value Decompositions (SVD)

by

Allison Liu

B.S., University of Colorado Boulder, 2022

A thesis submitted to the

Faculty of the Graduate School of the

University of Colorado in partial fulfillment

of the requirements for the degree of

Master of Science

Department of Applied Mathematics

2023

Committee Members:

Natasha Flyer, Chair

Elizabeth Bradley

James Meiss

Liu, Allison (M.S., Applied Mathematics)

Event Detection in Spatio-Temporal Data Using Singular Value Decompositions (SVD)

Thesis directed by Dr. Natasha Flyer

The ultraviolet (UV) and extreme ultraviolet (EUV) images taken by the Atmospheric Imaging Assembly (AIA) onboard NASA's Solar Dynamics Observatory (SDO) image different layers of the solar atmosphere and change more dynamically than magnetograms, which are the primary data source used for solar flare prediction. There is a need to understand the extent to which AIA image data can be used to enhance operational flare prediction methods. However, in order to do so, we must first be able to identify flaring events within the spatiotemporal AIA image data. Furthermore, we aim to understand patterns in solar flare precursor activity (known as microflares) leading up to large flare events of magnitude M1 or greater ($\geq 10^{-5} \frac{W}{m^2}$). Specifically, we use singular value decompositions (SVDs) of summed solar active region patches (SHARPs) taken by AIA to decompose the data into spatial and temporal modes, generating one-dimensional vectors which can be treated as time series signals. Our results show that there exist(s): (i) an underlying isotropic nature to the spatiotemporal data, (ii) peaks in the resulting SVD signals which align with flares defined in existing flare catalogs, and (iii) more precursor activity for M1-M4 and M5-M9 flares than for X flares.

Dedication

This thesis is dedicated to my parents, whose sacrifices gave me everything.

To my mom，Brenda 何月分，for her strength and endless support.

To my dad，Bruce 劉勛宇, who is still alive in the memories of everyone he taught about living.

Acknowledgements

I am so grateful for all that I have learned in the process of writing this thesis. It would not have been possible without the help of many people. First, thank you to Professor Elizabeth Bradley for her generous support of this research, without whom I would not have had the opportunity to pursue this degree. Dr. Natasha Flyer has been the best advisor I could have asked for, who always approaches research with patience, excitement, and creativity. It is rare to have an advisor who cares as much about her students as she does her work. Both of these women have been role models to me, pursuing research with dedication and rigor. I would also like to thank Dr. Tom Berger and Dr. Kiera van der Sande for the insightful discussions about the Sun and group meetings that always brightened my day. My previous research mentors Dr. David Couch and Dr. Wendy Carande continue to inspire me to solve problems in science and taught me invaluable skills.

This experience would not have been nearly as enjoyable without the incredible community of people I have around me. I am especially thankful to Callum Douglass, Alex Boehm, Anna McTigue, Nate Holland, and Hannah Martin for their feedback, providing me with new perspectives, and filling my life with adventure. My dad, Bruce Liu, never got to see me complete this degree, but remains one of my biggest inspirations. He encouraged me to chase my dreams, while never letting me forget that how I treat others is most important. People often liken me to my mom, Brenda He. It is the greatest compliment I could get. She is endlessly selfless, resilient, and hardworking, and has always been my biggest supporter. My brother Curtis reminds me to enjoy the little moments. Finally, I could not have done this without Kyle Fridberg and his unwavering encouragement during the most joyful successes and the difficult failures.

Contents

Chapter

Tables

Table

Figures

Figure

Chapter 1

Introduction

The problem of detecting anomalous events in spatiotemporal data commonly arises in geo-physical datasets. It is necessary to reliably forecast natural hazards to issue warnings to the public and prevent structural damage and loss of human life. In 2022 alone, 165 billion dollars in damage was caused by 18 different extreme weather events in the United States [48]. As such, there is extensive literature related to improving the prediction of events like earthquakes [44], avalanches [13], floods [40], volcanoes [42], and solar flares [6]. Detecting these natural phenomena remains difficult due to the complexity of the underlying causes and infrequent occurrence. The relative rarity of these events leads to imbalanced datasets, making detection and prediction challenging. Furthermore, because these natural events change dynamically on a quick timescale relative to the recorded data history, it is complicated to track and identify them in the spatiotemporal datasets.

Within the field of heliophysics, we consider the problem of solar flare detection. Solar flares are explosive bursts of electromagnetic radiation originating from the atmosphere of the Sun and can last from minutes to several hours [47]. Flares are highly correlated with coronal mass ejections [19] and geomagnetic storms which can cause disruptions in the Earth's magnetosphere [34][30]. Such changes in the magnetic field have the potential to damage critical infrastructure like the power grid and satellite communications [1]. Additionally, radiation associated with solar flares is harmful to astronauts in space, who are not protected by the Earth's atmosphere. Since even a 30 minute warning can prevent potential damage to infrastructure, it is critical to predict solar flare events in real-time. Due to the impacts of solar flares on human activity, detecting solar flare events

accurately and distinguishing between weak events and strong events that can cause damage is of great interest.

Onboard NASA's Solar Dynamic Observatory (SDO), which has been operational since 2010, there are two instruments that capture solar images at regular time intervals. The Helioseismic Magnetic Imager (HMI) captures full-disk solar magnetograms, or images of the magnetic field of the Sun. The Atmospheric Imaging Assembly (AIA) collects full-disk images of the Sun in multiple ultraviolet (UV) and extreme ultraviolet (EUV) wavelengths. The solar structure changes more dynamically and on a much shorter timescale in the UV/EUV wavelengths compared to the magnetic field, making it desirable as a direct source for identifying flaring events. In AIA images, flares appear as bright flashes of light. Flaring occurs in regions of the Sun with strong magnetic fields, called active regions (ARs). For this study, we consider time series of AIA images, which provides us with a 3-dimensional (2D in space plus 1D in time) spatiotemporal datacube of solar events.

Solar flare activity varies greatly with the 11-year solar cycle. At the peak of a solar cycle, up to several solar flares per day can occur. At solar minimum, we observe fewer than one per week [1]. However, while solar flares occur relatively often, events which have the potential to affect human operations on Earth occur much more infrequently (only 750 flares in Solar Cycle 24 2008-2019). Compounded with the fact that there are often gaps in sensor data, and that flares captured while on the limb of the Sun may not be directly comparable to flares on the face because of intensity differences in the images, this lack of positive flaring instances presents a problem for both solar flare prediction and detection. There are simply not enough events to identify conclusive patterns in the data leading up to an event. The explosive events are also difficult to locate within an AIA image due to the constant background activity on the surface of the Sun.

The most extensive catalog of solar flares is captured by the Geostationary Operational Environmental Satellites (GOES) which are a series of satellites monitoring the Earth and operated by the National Oceanic and Atmospheric Administration (NOAA). Solar flares are classified by

their peak X-ray flux as measured by the GOES satellites. The GOES X-ray flare catalog[1] contains a detailed history of significant flares dating back to 1975, but the single value definition of flares does not retain any spatial information. Additionally, the catalog is missing AR labels for many of the flares and does not contain any entries describing small events that could act as precursor signals.

It has been well-established that large flare events are often preceded by precursor flares [49]. Precursor flares can range in size from large flares to ones much smaller than the flare of interest, which are called microflares. We define "large" flares as flares with a measured peak X-ray flux greater than $5 \times 10^{-5} \ W/m^2$. This is the baseline for the Space Weather Prediction Center (SWPC) to issue an alert to the public [1]. Studies have demonstrated that the occurrence of a flare increases the likelihood of another event [20]. Thus, the first major event in a series is the most important to predict. *This thesis aims to study the time period leading up to large solar flares and identify patterns in microflares during this time.* Techniques from this study have the potential to be used for detecting rare events in other spatiotemporal datasets.

In this work, we introduce the concept of using singular value decompositions (SVDs) for spatiotemporal event detection. In Chapter 2, we present relevant literature for spatiotemporal event detection, focusing on solar flare events. Chapter 3 describes the EUV/UV solar image data utilized for this study. In Chapter 4, we discuss methodology used for identifying and understanding events preceding large solar flares. We first transform the solar image data into time series by summing images into 1D vectors to create a matrix with rows representing space and columns representing time. We then perform an SVD on the resulting matrix to decompose it into spatial and temporal components. Chapter 5 describes results obtained from analysis of the singular vector signals. Finally, we summarize our results and discuss future work in Chapter 6.

---

[1] https://www.ngdc.noaa.gov/stp/space-weather/solar-data/solar-features/solar-flares/x-rays/goes/xrs/

Chapter 2

Background Literature

The following section reviews some commonplace mathematical and computational techniques in the literature for identifying events in spatiotemporal data. The section concludes with a discussion of the literature pertaining to the relationship between precursor activity and the solar flare events of interest.

2.1 Techniques for Event Detection in Spatiotemporal Data

Methods for spatiotemporal event detection have been extensively studied in image processing, statistics, and machine learning [55]. Upon identification of target events, pattern recognition can be used to extrapolate information and predict future events.

Statistical techniques: These techniques use statistically significant patterns in the data to make conclusions about features such as mean pixel value, time to event, and event location. Earthquake precursor identification has involved analyzing precursor signals in seismological data [31] and shares many similarities with the task of solar flare identification. In [14], the distributions of various properties of earthquake precursor signals (spatial extent, time, duration, amplitude) were analyzed and used to correlate precursor activity with earthquake magnitude. They determined that precursor activity increased closer to the earthquake epicenter. Another study derived features from solar magnetograms and used discriminant analysis, a statistical technique that uses probability density functions to determine which group a given observation belongs to in order to predict solar flares [7]. Wheatland estimated the probability of a solar flare using a Bayesian approach

to fit a probability distribution based on flare statistics [53]. While computationally very efficient, statistical features are often human-determined and do not provide an adequate description of spatial information present in data. Statistical techniques also assume that the sample of data is representative of the population and tend to be more useful with large datasets [18].

Mathematical/Computational techniques: In time-frequency analysis, the factorization of spatiotemporal data into spatial and temporal modes is known as the blind source separation (BSS) problem. Given a signal which proceeds in space and time, the goal is to recover the underlying signals which compose the data. A large family of methods including the Fourier transform and the singular value decomposition (SVD) exist for solving the BSS problem [28] by decomposing the data into a set of components. In the context of geophysical signal processing, diffracted seismic signals can be used to identify regions of geologic interest like faults and fracture zones. As these diffracted signals are weaker, they can be masked by other stronger signals. SVDs have been used to improve the accuracy of geologically heterogeneous zones by extracting these diffracted signals from waves [46]. BSS methods have also been used to improve event detection. For example, it is possible to detect cyber-attacks on water distribution systems by separating time series using fast Independent Component Analysis (fast ICA) related to water tank pressure into independent components and analyzing them for abrupt changes using a statistical control algorithm [10].

Object-based image processing methods rely largely on background subtraction to detect and track objects as they move through image frames. For example, in [38] the authors track detected objects over sequences of images by matching regions and inferring their trajectories over time. [32] presents a summary of background subtraction-based object detection methods. In contrast, other techniques leverage topological properties (e.g. connectivity, compactness, shape) which are not considered in object-based methods [11]. For solar flare prediction, topological features perform equally as well as parameter-based features [17]. Unfortunately, many object detection methods still rely on human-identified regions of interest [9]. Image-based event detection remains difficult in geophysical data due to the ill-defined boundaries of naturally-shaped objects such as tornadoes and bodies of water [33].

Machine learning techniques: Machine learning methods for event detection can be divided into two subcategories: supervised and unsupervised. Statistical and image processing techniques provide useful training features for machine learning models. Supervised methods require data with labels to produce models. It is often costly and time intensive to create labeled datasets. However, supervised models generally produce more accurate results compared to unsupervised ones. Examples related to event detection include the development of a predictive modeling framework for identifying forest fires in urban areas using poorly labeled satellite data [39] and the use of generative adversarial networks to identify flood events from images [43]. An Extremely Randomized Trees regression model was used to identify solar flares from solar images [51]. Unsupervised methods do not require labeled datasets, instead relying on unspecified properties within the data to find inherent patterns. One study used k-means clustering to classify volcanic events from seismic signals [29]. Another used genetic algorithms for detecting water system contamination [3]. Solar flare precursor signatures were identified using observed changes in spectral profiles of the Sun and K-means clustering [54].

2.2 Relating Precursor Activity to Solar Flare Events

There is a considerable amount of literature showing that several solar flares often occur close together in time [35] and that large solar flares are commonly preceded by smaller precursor flares, known as microflares [27]. A comprehensive flare precursor study by Tappin postulates that many small precursors are indicative of regions of instability which may lead to flares [49]. The mechanism behind flaring is not well understood. Examining flare precursor data provides valuable insight into why and how solar flares occur.

There are many studies which identify a few flaring events and analyze the time period leading up those events in depth (Wang et al. [52], Harra et al. [26], Farnik et al. [21]). These case studies are helpful for understanding the relationship between flares and precursors as well as providing insight into flare onset mechanisms. However, it is not possible to generalize results across many solar flare occurrences as they only examine one or two flare instances.

Alternatively, many studies statistically analyze solar changes in the time period leading up to flare events (see [25] for a review). From a database of approximately 40,000 magnetograms, Falconer et al. finds evidence that prior flaring rate of an active region statistically impacts the likelihood of a large flare occurring [20]. Using a sample of 32 flares from October 1993 - October 1994, Farnik and Savy classified the spatial relationship between flaring events based on precursor information from the Yokoh satellite [22]. It has also been shown that flares of different sizes have different observed characteristics [16]. By studying the spatiotemporal flare distribution 24 hrs before large flares, Gyenge et al. showed that there are temporal differences in precursor activity depending on the strength of the flare. Flaring starts earlier in stronger flares and later in weaker ones. Additionally, in the 6 hrs immediately preceding a flare of interest, precursor flares follow a log-normal distribution [24]. However, over long periods of time, flaring events follow a power-law distribution independent of solar cycle [2], [15], [36], [4]. While these studies provide insight into patterns in the data for a given time period leading up to flares, they cannot establish explanations for causal relationships between flares and precursors. Thus, the literature to date remains very limited.

Chapter 3

Data

The images used in this solar flare study are full-disk UV and EUV images taken by the AIA onboard NASA's SDO. Solar flares are defined using the peak flux of soft X-rays (1-8 Å) in watts per square meter (W/m^2) as measured by the GOES satellites. Flares are classified using a logarithmic scale with the letters A, B, C, M, and X as in Table 3.1. For example, an M7 flare is one with a flux of 7×10^{-5} W/m^2. As shown in Figure 3.1, stronger flares (M and X) occur less frequently.

Class	Avg Peak Flux (W/m^2)
A	$< 10^{-7}$
B	$10^{-7} \leq$ B $< 10^{-6}$
C	$10^{-6} \leq$ C $< 10^{-5}$
M	$10^{-5} \leq$ M $< 10^{-4}$
X	$> 10^{-4}$

Table 3.1: Classification of solar flares by peak flux.

Source: https://www.swpc.noaa.gov/phenomena/solar-flares-radio-blackouts

In addition to the GOES X-ray flare catalog, another catalog of flaring events using solar images captured in UV and EUV wavelengths has recently been created. The AIA catalog captures an overlap of 85% M/X flaring events with the GOES flare catalog and identifies previously unrecorded flares, as well as C flares (which are not identified by GOES) [51]. We verify our identification of flares with those from this new AIA catalog.
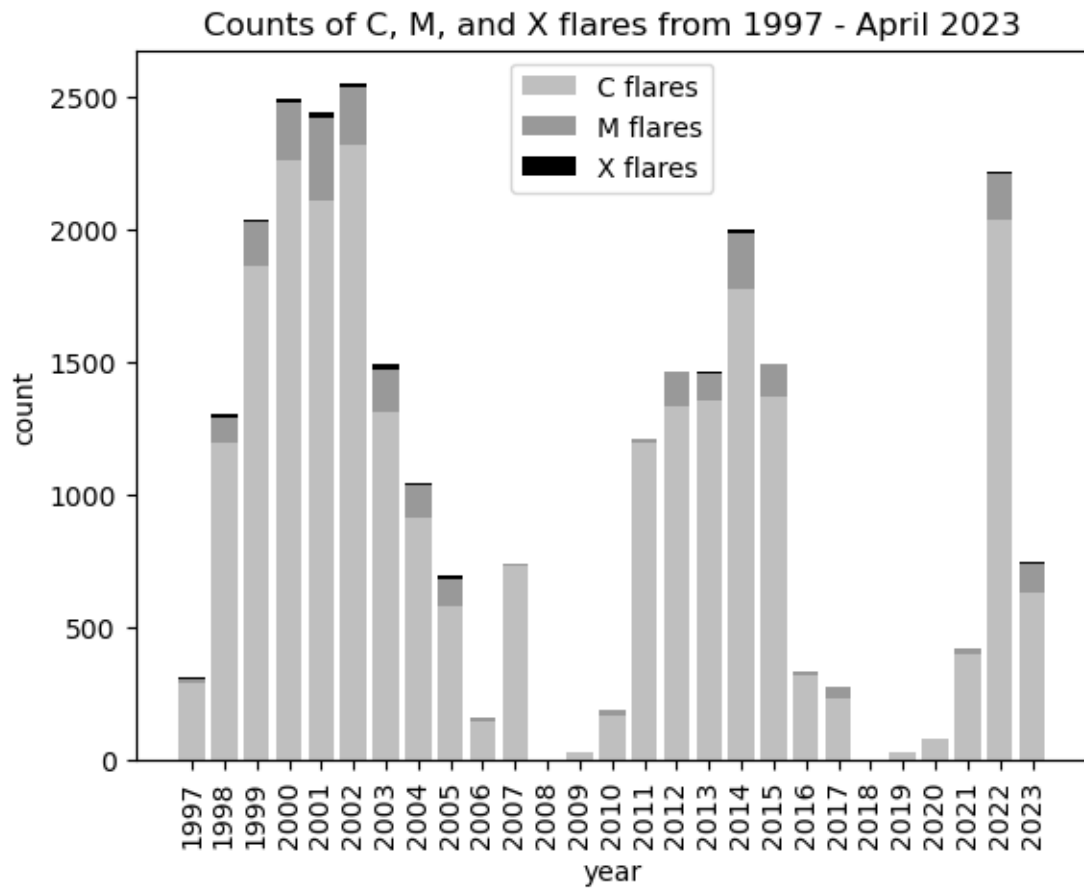
Figure 3.1: A plot of the number of solar flares by class that have occurred from 1997-2023 (present).

3.1   Time Series Images

AIA collects images of the Sun in wavelengths ranging from 94 Å to 4500 Å at a 12 second cadence. Many studies use cutouts of active regions of the Sun, known as Spaceweather HMI Active Region Patches (SHARPs) [8]. For this study, we use active region cutouts derived from the original AIA images that are congruent with the magnetogram SHARPs. These cutouts are constructed via the procedure given in [51]. We refer to these AIA cutouts as "AIA SHARPs". Structures in AIA images change more dramatically and on a shorter time scale compared to HMI magnetograms. Images of the Sun are taken using different AIA wavelengths, which capture emissions from different layers of the solar atmosphere 3.2. Although it is common in the literature to focus on the following six wavelength channels (94 Å, 131 Å, 171 Å, 193 Å, 304 Å, 1600 Å), we concentrate on the 131 Å and 94 Å channels. It was shown that features derived from these two channels played the most important role in predicting AIA flare magnitudes [51]. Figure 3.2 shows an example of an active region cutout of SHARP 7115 for a magnetogram and five AIA wavelengths.
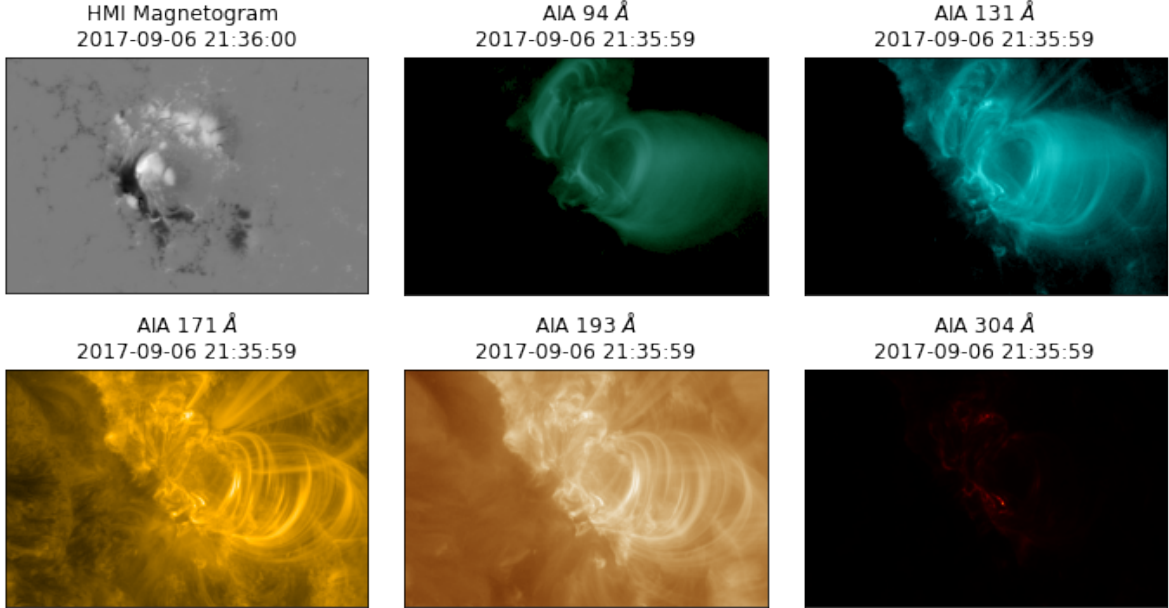

Figure 3.2: A plot of AIA images in 5 wavelengths (94 Å, 131 Å, 171 Å, 193 Å, 304 Å) and an HMI magnetogram for SHARP 7115. The images at this timestep occur approximately 8 hrs and 36 mins before an M2.4 flare and 5 hrs and 45 mins after an M2.5 flare.

Wavelength (Å)	Region of solar atmosphere
94	flaring regions
131	flaring regions
171	quiet corona, upper transition region
193	corona and hot flare plasma
304	chromosphere and transition region
1600	transition region and upper photosphere

Table 3.2: Regions of the solar atmosphere observable by six AIA wavelength channels.

Source: AIA Instrument Website - https://www.lmsal.com/sdodocs/doc/dcur/SDOD0060.zip/zip/entry/

We consider SHARPs beginning in 2010, when SDO became operational, until 2017, when Solar Cycle 24 approached solar minimum. We are interested in characterizing the time period leading up to large solar flares, that is flares of magnitude greater than or equal to M5 (5×10^{-5} W/m^2), as defined by the AIA-based flare catalog [51]. Rather than using X-ray flux, the AIA-based flare catalog determines flare magnitudes using total summed intensity from the AIA images directly. After removing flares which occur on the limb of the Sun and accounting for missing data, we are left with 57 flares greater than or equal to M5 across 27 different SHARPs, recalling that M5 is the minimum flare magnitude for which SWPC issues an alert. Table 3.3 lists the flare counts for each catalog.

Flare Catalog	X	M5 - M9	M1 - M4	C
GOES	23	43	328	2242
AIA-based ERT	25	39	355	15687

Table 3.3: Total flare counts for Solar Cycle 24 by flare class.

3.2   Sample Creation

We define a sample as data collected during a time period of a fixed length preceding a solar flare of interest. For this study, we consider flares of interest as flares of magnitude greater than or equal to M1. While M5 is the baseline for SWPC to issue an alert, weaker M1 - M4 flares are of interest from a research perspective in the literature. Considering M1-M4 flares also results in more samples, as there are considerably more M1-M4 flares than M5+ flares. Additionally, in the

prediction literature, scientists are interested in a 12 hr time period before a flare for short-term prediction [17] [41] [12]. Thus, we consider samples of a fixed 12 hr window preceding flares greater than or equal to M1. We remove samples containing an M5 or greater flare, as M5 flares are no longer precursors. After removing samples that are overlapped in time by more than 20%, we obtain the following sample counts:

total samples	X flares	M5 - M9 flares	M1 - M4 flares
104	20	26	58

Table 3.4: Sample counts for X, M5-M9, and M1-M4 flares from SHARPs without flares greater than or equal to M5 in Solar Cycle 24.

In Solar Cycle 24, there are 25 X-flares in total (Table 3.3). Of the five unaccounted for X-flares in Table 3.4, four occur directly after another $\geq$ M1 flare and one occurs on the limb of the Sun, making the intensity not consistent with other flares of similar magnitude.

Chapter 4

Methodology

In the below subsections, we describe how to manipulate the flare data to create a space-time matrix. We then introduce the concept of using SVD for spatiotemporal event detection.

4.1 Space-flattening of the Data

Within the field of information visualization, many models and nomenclature exist for transforming three-dimensional spatiotemporal datacubes. Transformations of the data can allow for more intuitive or descriptive interpretations of information. Our datacube consists of two spatial dimensions and one temporal one: (x, y, t). "Space-flattening" refers to flattening the datacube along either the x or y axis (in our case, longitude or latitude, respectively) so that we are left with a 2D plane, either (x, t) or (y, t) [5]. Given a time series of images, this can be interpreted as summarizing each image by obtaining a "slice" or cross-section cut of it.

For each SHARP, in the wavelengths considered, we begin with a time series of images, as in Figure 4.1. To space-flatten the data, we proceed in the following steps as illustrated in Figure 4.4

(1) Subsample the AIA SHARP images at a 12 min cadence.

(2) Sum either across rows or down columns (Figure 4.2) to obtain a 1D vector for each image.

(3) For each 1D vector, center and crop around values which are greater than 60% of the maximum intensity value to obtain a uniform vector length.

(4) Combine these signals to form a single 2D matrix representing each SHARP (Figure 4.3). We will refer to this matrix as the **"summed SHARP matrix".**

Following steps 1 through 4 transforms the data so that spatiotemporal features can be analyzed via an SVD, as discussed in the next section. In the section that follows, examples are shown using row-summed SHARP matrices. In Chapter 5, we will discuss the natural spatial invariance observed when summing across rows and down columns.
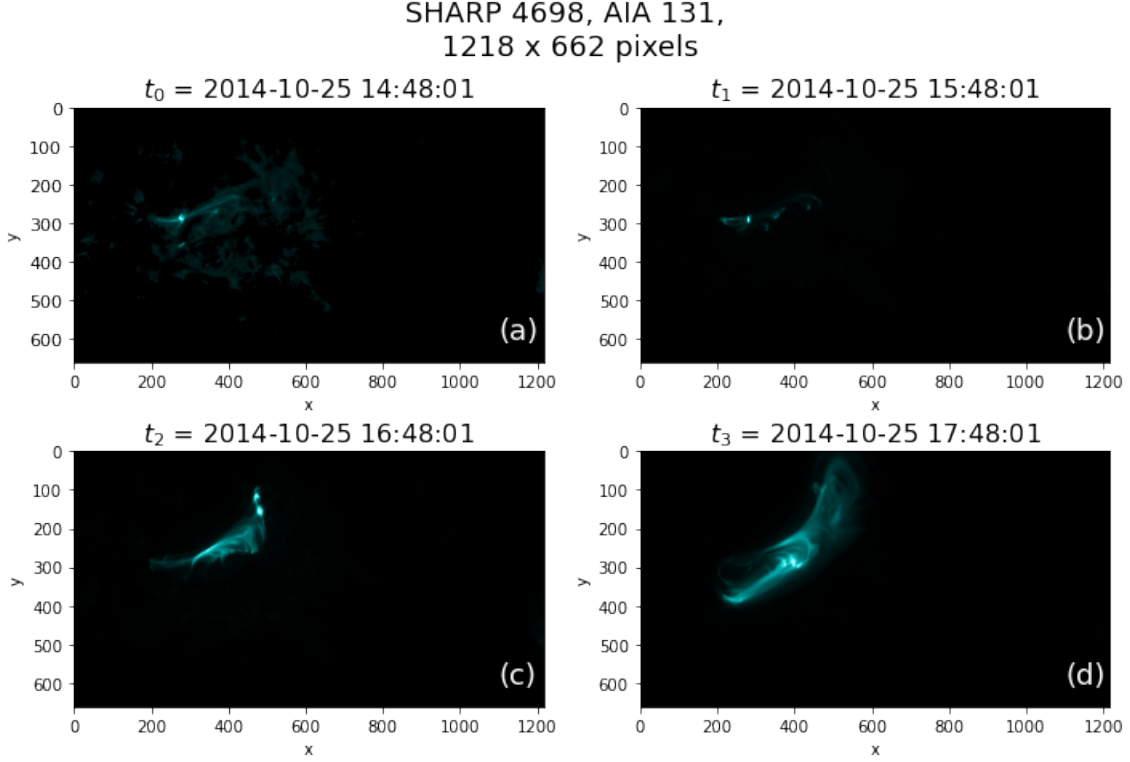

Figure 4.1: An example of four AIA images taken using a wavelength of 131 Å for SHARP 4698 with a cadence of 1 hr. An X1 flare occurs 4 minutes after the image in (c).

4.2   Singular Value Decomposition

The singular value decomposition (SVD) is the one of the most ubiquitous matrix factorizations in linear algebra. An SVD of a matrix $M \in \mathbb{R}^{m \times n}$, returns a decomposition of the form

$$M = U \Sigma V^*$$

where U is a unitary matrix that relates to the row space of M and similarly V relates to a unitary decomposition of the column space of M [23]. As such, in the case that the rows of M represent space and the columns represent time, the left singular vectors u_i that compose the columns of U

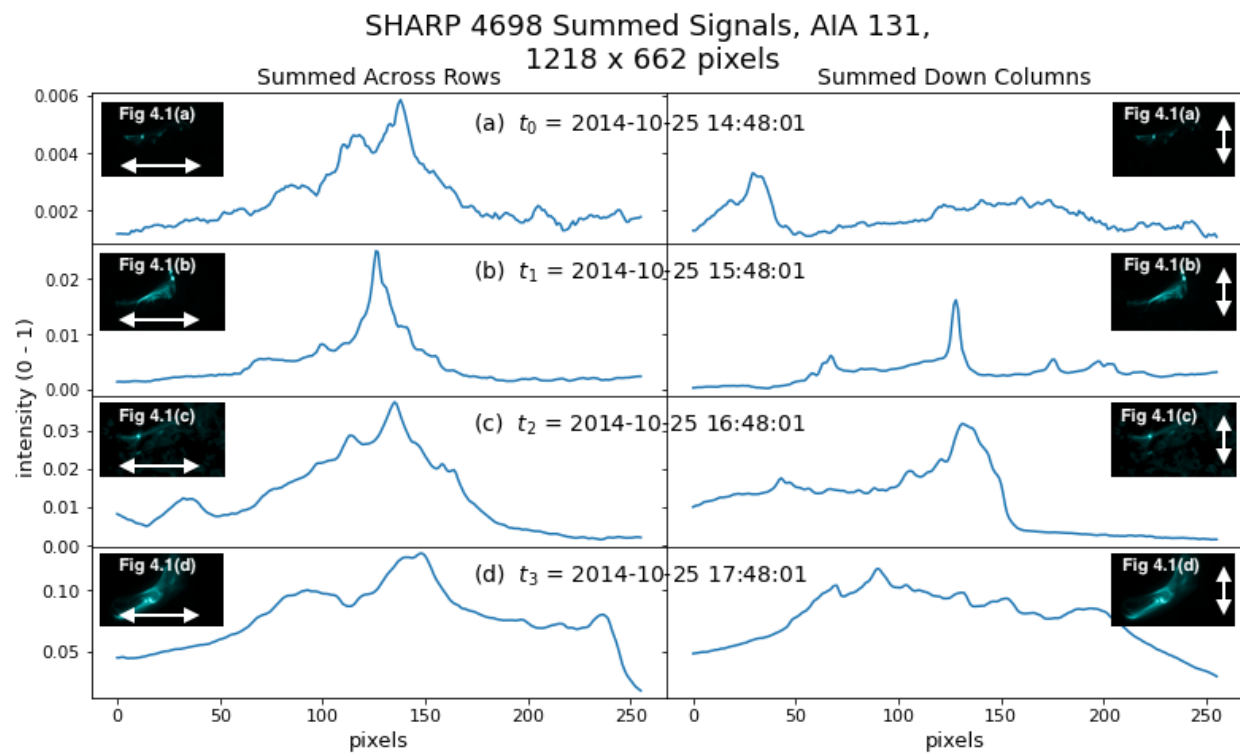Figure 4.2: The 1D vectors created by summing the images in Figure 4.1 across rows (left) or down columns (right), and then cropping to obtain vectors of length 256.
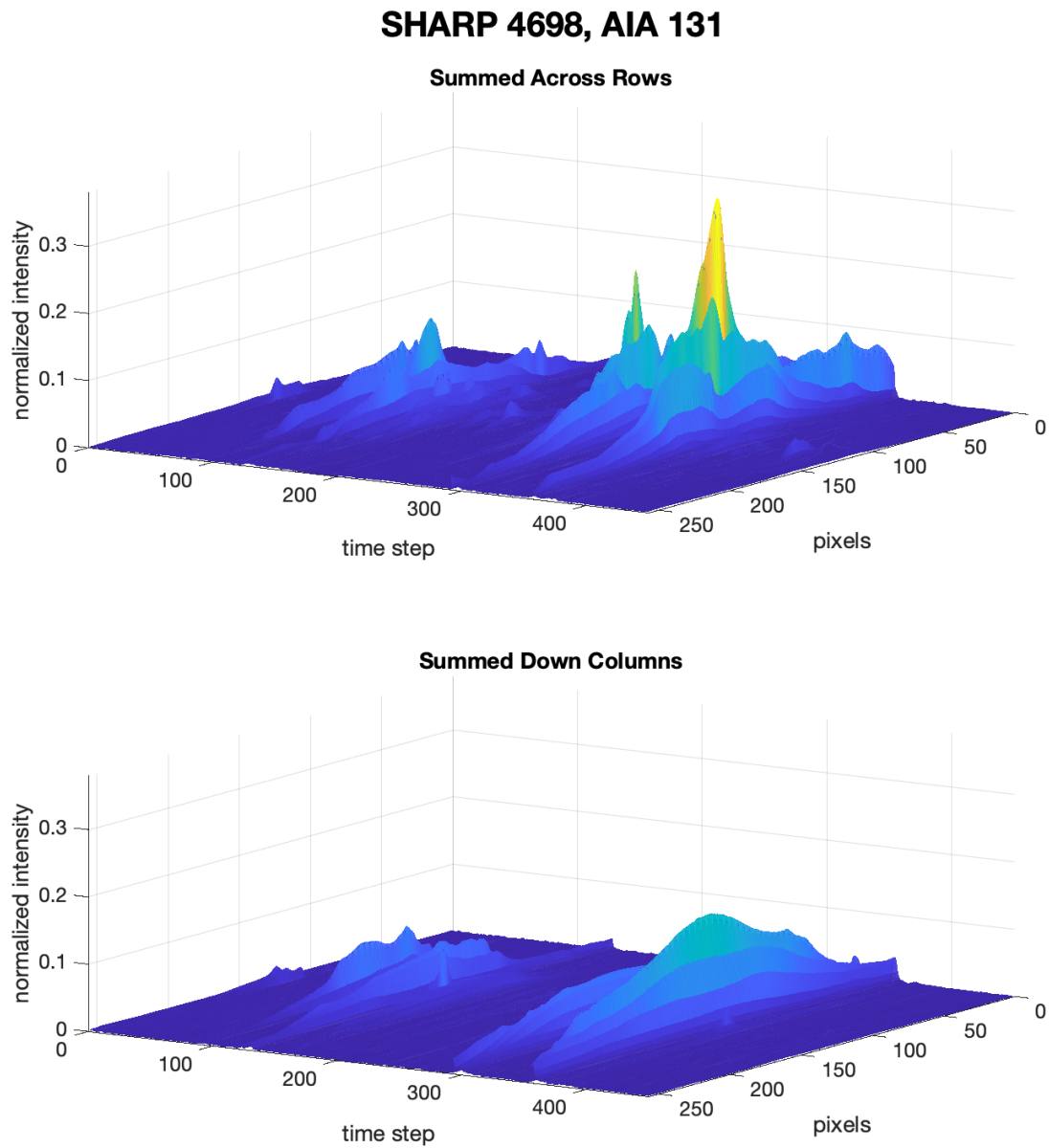
Figure 4.3: A surface plot of the matrix produced by summed images in AIA 131 Å for SHARP 4698. Every 10 time steps represents 2 hrs.
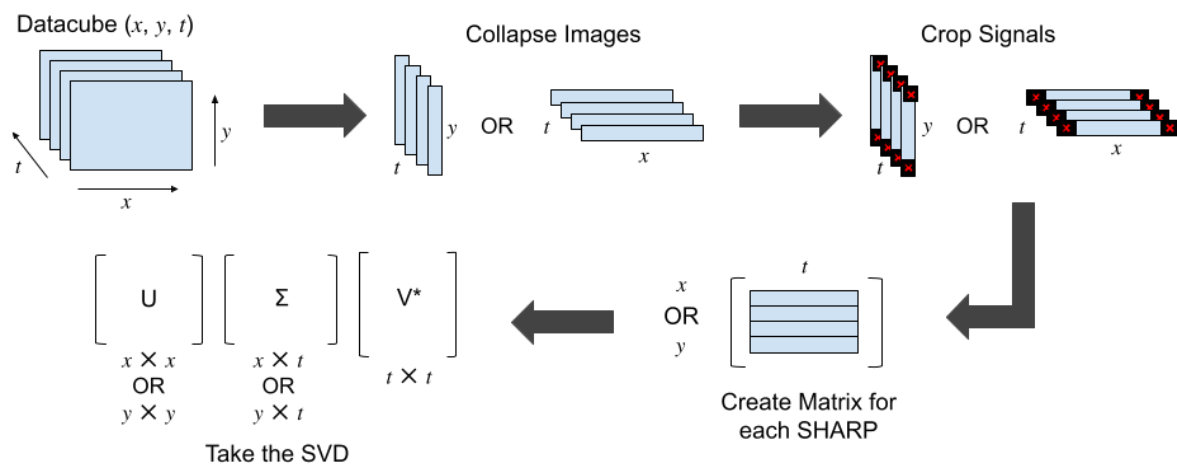
Figure 4.4: The series of data transformations taken to extract spatial and temporal modes from a time series of AIA images.

can be interpreted as spatial modes of M and the right singular vectors v_i that compose the columns of V can be interpreted as temporal modes. The matrix Σ is diagonal and contains the singular values which are scalar coefficients of the corresponding singular vectors. It is standard to order the singular values σ_i (with their corresponding singular vectors) such that $\sigma_1 \geq \sigma_2 \geq \cdots \geq \sigma_n \geq 0$.

For each SHARP, we create a summed SHARP matrix as shown in Figure 4.3, where the rows represent pixel number and the columns represent time. We then take the SVD of the summed SHARP matrix and obtain singular values as shown in Figure 4.5. Based on the singular values, the contribution of each singular vector can be determined. Notice that the singular values decay exponentially (Figure 4.5). By the ninth singular value, σ_9 is only 3.88% of σ_1.
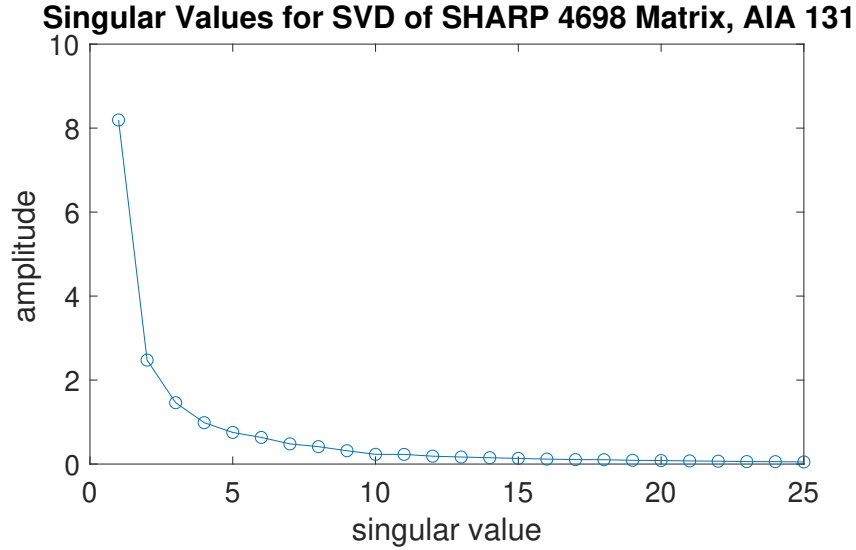
Figure 4.5: The first 25 singular values obtained from the SVD of the summed SHARP 4698 matrix (summed across rows).

U vectors for SHARP 4698, AIA 131

$\sigma_1 = 8.1926$

$\sigma_2 = 2.4756$

$\sigma_3 = 1.4607$

$\sigma_4 = 0.98576$

$\sigma_5 = 0.75281$

$\sigma_6 = 0.63405$

$\sigma_7 = 0.48067$
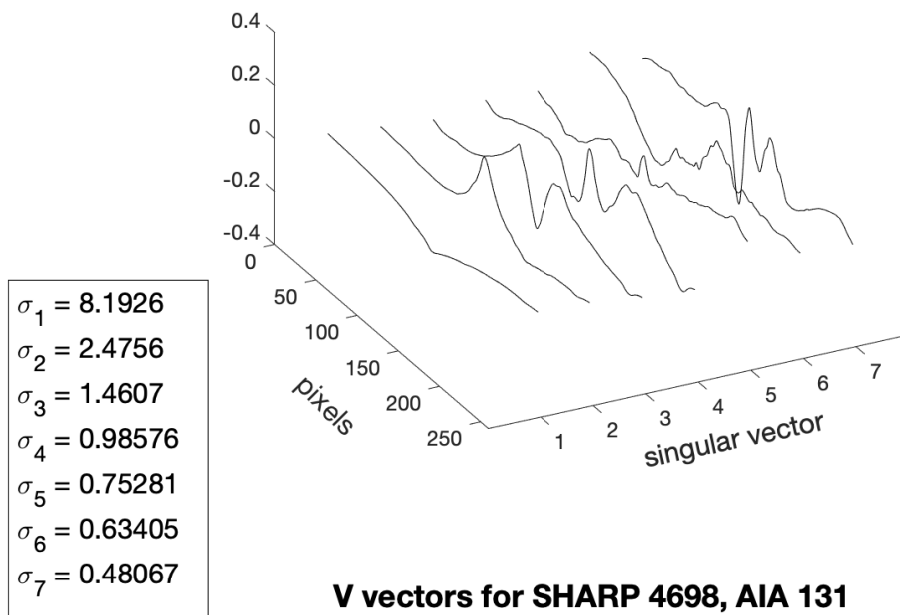
V vectors for SHARP 4698, AIA 131

Figure 4.6: The first seven singular vectors of the U and V matrices (i.e. the columns of U and V) obtained from taking the SVD of the summed SHARP 4698 matrix (summed across rows) in Figure 4.1.

As stated above and shown in Figure 4.6, the SVD gives an orthonormal decomposition of the spatial and temporal phenomena represented in the summed SHARP matrix into the U and V singular vectors, respectively. Figure 4.4 shows the series of transformations taken to decompose the 3D datacube of images in time into spatial and temporal modes represented by the singular vectors. The amplitude of the singular vector v_i at a given time represents t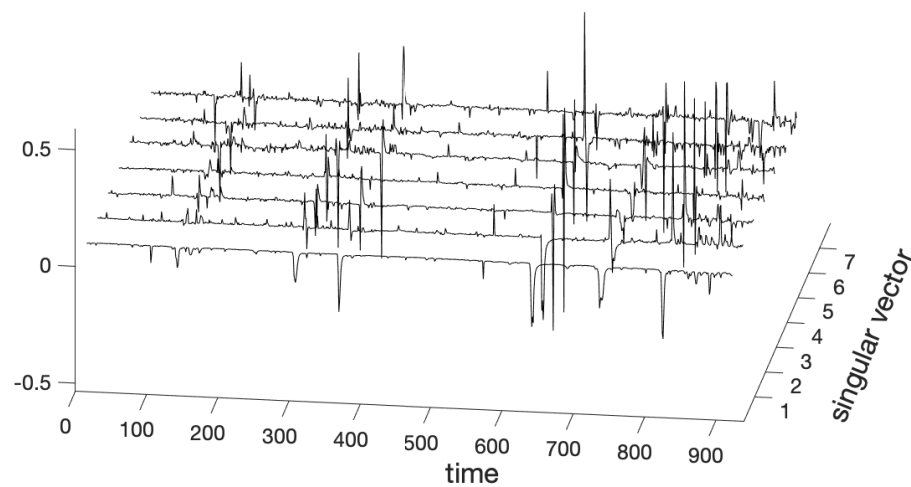he quantity of the spatial component u_i that is present at a given time, scaled by the singular value σ_i. We leverage these two properties in understanding features corresponding to solar flares that appear in the resulting right singular vectors $v_1, \ldots, v_n$ of our data matrix to obtain a time series. The SVD for the same SHARP appears slightly different in each wavelength as a result of flaring occurring at different times in each layer of the solar atmosphere.

Given that SVDs have been used to separate spatial and temporal modes in data [28] and that it is difficult to effectively preserve spatial structure in time series images for event detection, the goal of this work is to analyze the time period preceding major solar flares to attempt to answer the following questions: (1) Can we devise a method to identify microflares in image data preceding a major solar flare while preserving spatial information? (2) Using this method, is there a pattern in precursor flares observable in the resulting signals?

Chapter 5

Results

Taking the SVD of each of the 27 SHARPs with flares greater than or equal to M5, we analyze the properties of the singular vectors from the resulting 27 V matrices which are treated as time series. Furthermore, through our analysis of the precursor activity exhibited in the singular vectors, we are interested in identifying three classes of flares: X, M5 - M9, and M1-M4.

5.1   Invariance of Results to Summing Rows or Summing Columns

In Chapter 4, we sum a time series of images either across rows or down columns to obtain a summed SHARP image, as demonstrated in Figure 4.3. Due to the anisotropic appearance of the AIA images (as can be seen in Figure 4.1) and the differences in the structure of the two matrices, we expect the singular vectors of the two matrices to be different when we take their SVDs. Instead, we obtain singular vectors that appear very similar regardless of which axis the image is summed along. While the amplitudes of the peaks may differ, the peaks of the signals align well in the temporal dimension across all singular vectors. For example, in SHARP 5298, for the M3.7 flare which occurs at approximately timestep 130, the summed down columns (dashed gray curve) peak increases in height relative to the summed across rows peak (black curve) as the singular vectors increase while the peaks remain in line (Figures 5.1, 5.2, 5.3). Even the smaller features, which are recovered from the original images in higher singular vectors, align just as well as those in lower singular vectors. This observed isotropy in the singular vectors is surprising, as it reveals that taking the SVD of the AIA SHARPs is spatially invariant. We note that for singular vectors corresponding

Figure 5.1: Singular Vector 2, v_2, of the V matrix resulting from taking the SVD of the summed SHARP matrices for SHARPs 1449, 4698, 5298, and 7115.

to higher singular values, creating the SHARP matrix by summing across rows compared to down columns leads to slight deviation in amplitude of the fine structure within the vectors. From these experiments, we conclude that the summed AIA SHARPs are quasi-isotropic.

Figure 5.2: Singular Vector 5, v_5, of the V matrix resulting from taking the SVD of the summed SHARP matrices for SHARPs 1449, 4698, 5298, and 7115.
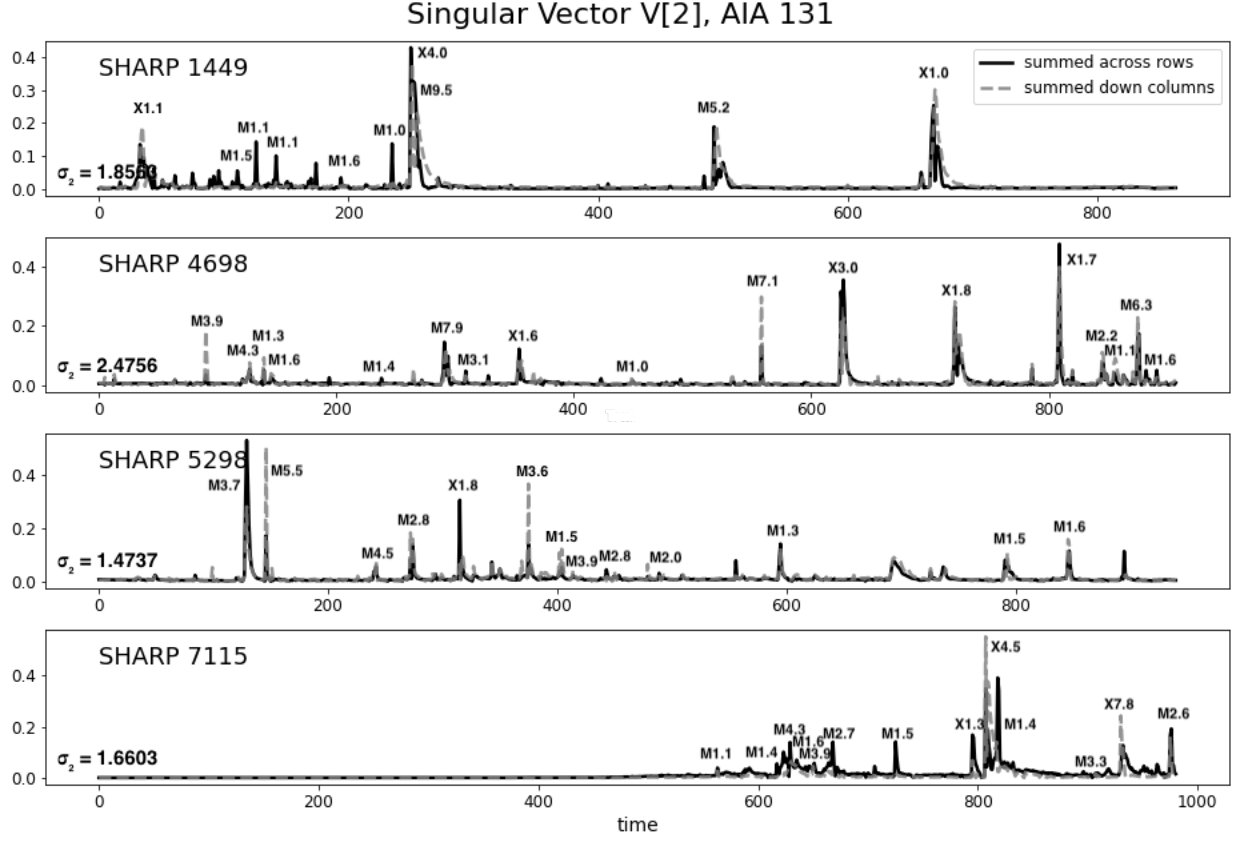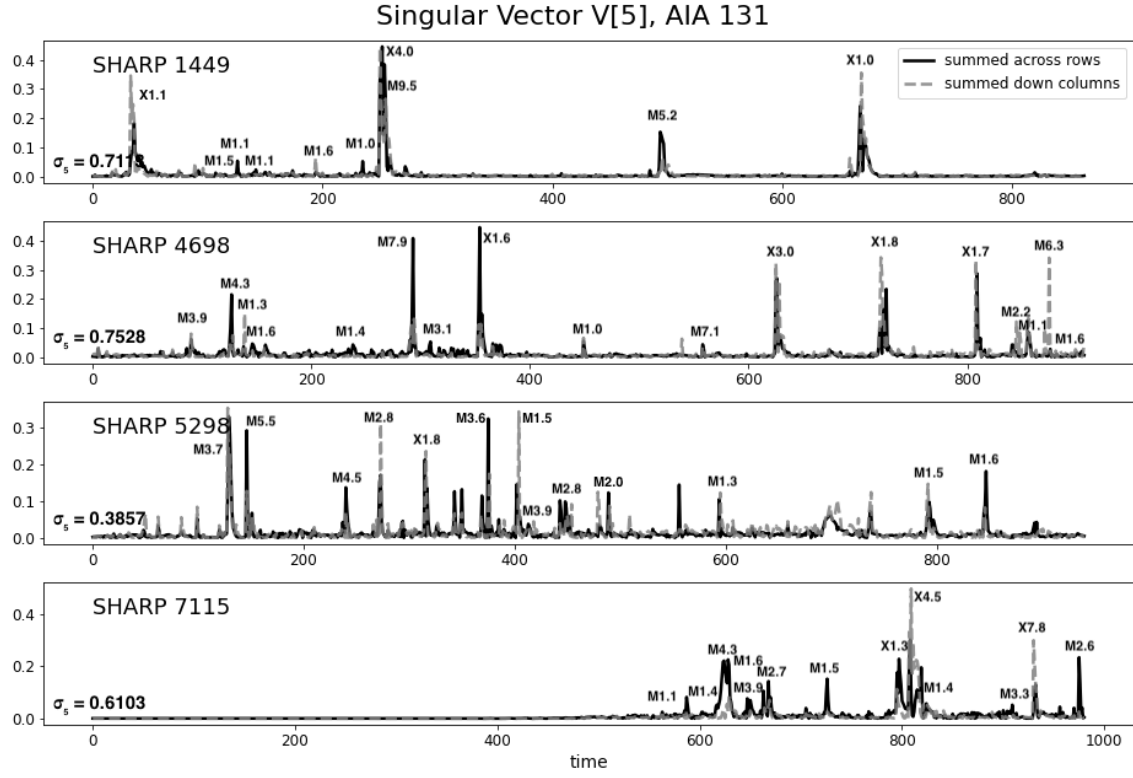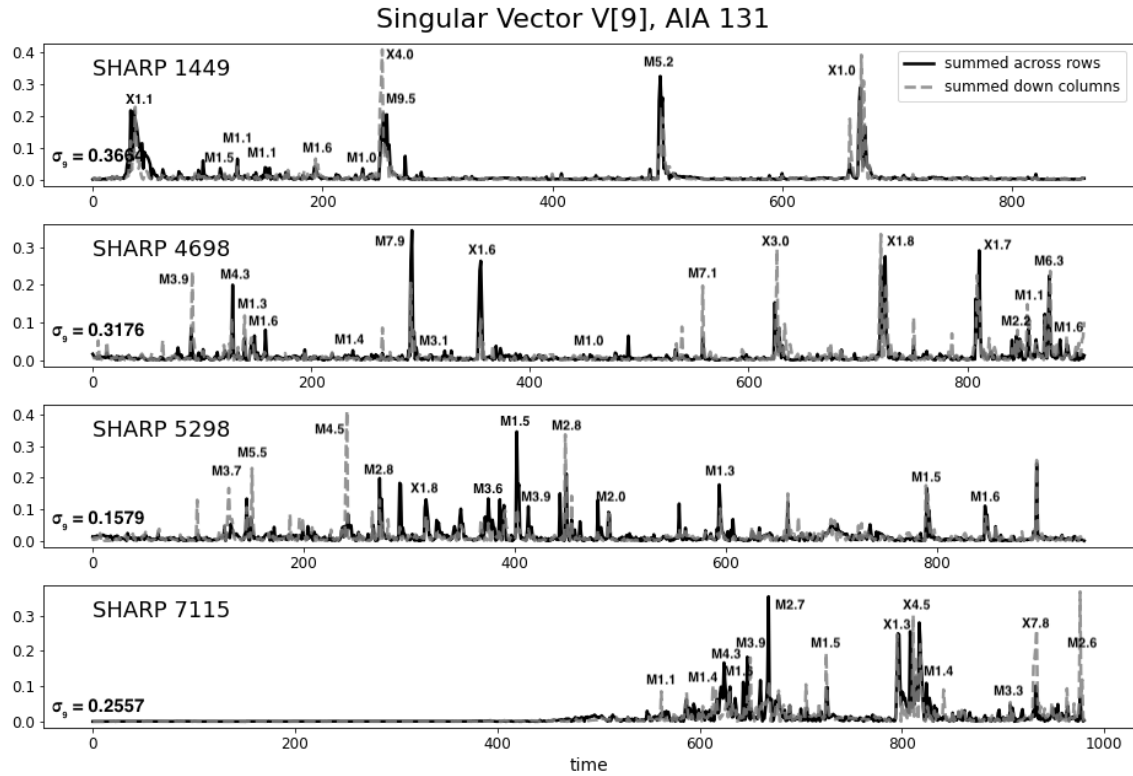

Figure 5.3: Singular Vector 9, v_9, of the V matrix resulting from taking the SVD of the summed SHARP matrices for SHARPs 1449, 4698, 5298, and 7115.

5.2   Consistency of Singular Vector "Events" with AIA Flare Catalog

For flares for which SWPC would issue an alert to the public (greater than or equal to M5), we find that flare events line-up exactly with peaks in the resulting singular vector signals. It is helpful to keep Figure 4.6 in mind, recalling that we have a *U* and *V* matrix composed of singular vectors for each SHARP. Across SHARPs, the tall peaks tend to represent flares greater than or equal to M5, with a few exceptions. In general, we observe that the width of the peaks corresponding to large flares are more defined and taller in the 1st and 2nd singular vectors. In contrast, the precursor C and smaller flares become much more prominent (relative to the large flare peaks) after the 4th singular vector. The size of the microflare peaks relative to the size of a solar flare of interest is amplified in these singular vectors, revealing previously undetected structure in the data. When using decompositions such as the SVD, one generally cares about the information in the data represented by the singular vectors corresponding to the singular values with the largest magnitude. *In this case, however, the information relevant to understanding microflares preceding large flares may be contained in singular vectors corresponding to smaller singular values.*

In Figures 5.4-5.7 and 5.10, the vertical lines represent flares defined by the AIA flare catalog. We see that the larger peaks tend to align with flares of greater magnitude, particularly in singular vector 1. For example, the M7.9 peak in Figure 5.4 is smaller in magnitude in singular vector 1 than the X1.6 flare. The X1.1 peak is smaller than the X4.0 peak in Figure 5.5. As the singular vectors increase, the M1-M4 peaks also increase in magnitude. For C flares, we also find this to be true. Figure 5.6 shows the same plot of singular vectors 1-9 as in Figure 5.4 zoomed into the 150-200th timesteps. Here, the C9.5 flare corresponds with the largest peak and small peaks exist where flares are defined by the AIA catalog.

Characterizing the magnitude of microflares using this SVD technique provides additional information compared to summing up pixel intensities in AIA images as in [51] as well as the GOES single-value definitions of flares based on X-ray flux. Having seen in Section 5.1 that large-scale spatial structures are invariant whether the images are summed across rows or down columns,

we deduce that this SVD technique preserves large-scale spatial information in at least one direction for each timestep.

Singular Vector	Information Content
1	Average of spatiotemporal data, smoothest
2-3	Corrections to averages of spatiotemporal data
4-10	Fine structure within the signals, each successive singular vector accounts for increasingly finer structure
approx 10+	Non-physical information, ensures orthogonality of matrix

Table 5.1: A summary of what we generally observe from each singular vector across SHARPs with large flares.

As discussed in Chapter 4, we consider samples of length 12 hrs (60 time steps) before M1 and greater flares. In total, we have 20 X-flare samples, 26 M5-M9 flare samples, and 58 M1-M4 flare samples which occur across 27 different SHARPs. Using singular vector 5, we show examples of two samples leading up to an X flare, an M5-M9 flare, and an M1-M4 flare. We notice the contrast in signals leading up to the two X flares, where the sample in Figure 5.7a has significantly more precursor activity compared to the sample in Figure 5.7b, which remains rather quiet in the 12 hrs before the X3.8 flare. In the signal leading up to the M6.4 flare, we see that the peak corresponding to the larger C9.9 flare is smaller than the peak corresponding to the C7.5 flare (Figure 5.7c). Similarly, the signal in Figure 5.7d has a peak corresponding with a C9.8 flare approximately 2 hrs (10 time steps) that is much larger than the peak for the M1.4 flare it precedes.

5.3 Correlating Precursor Activity to Magnitude of Solar Flare Event

Using the 104 samples of data captured 12 hrs before large solar flares, we examine the singular vector signals in an attempt to identify relationships between flare precursors and large solar flares. We note that due to a small sample size, this study remains rather qualitative in nature.

For each SHARP, we have as many singular vectors (of V) as there are timesteps in the data. We first determine which elements of the data can be understood by each singular vector. In
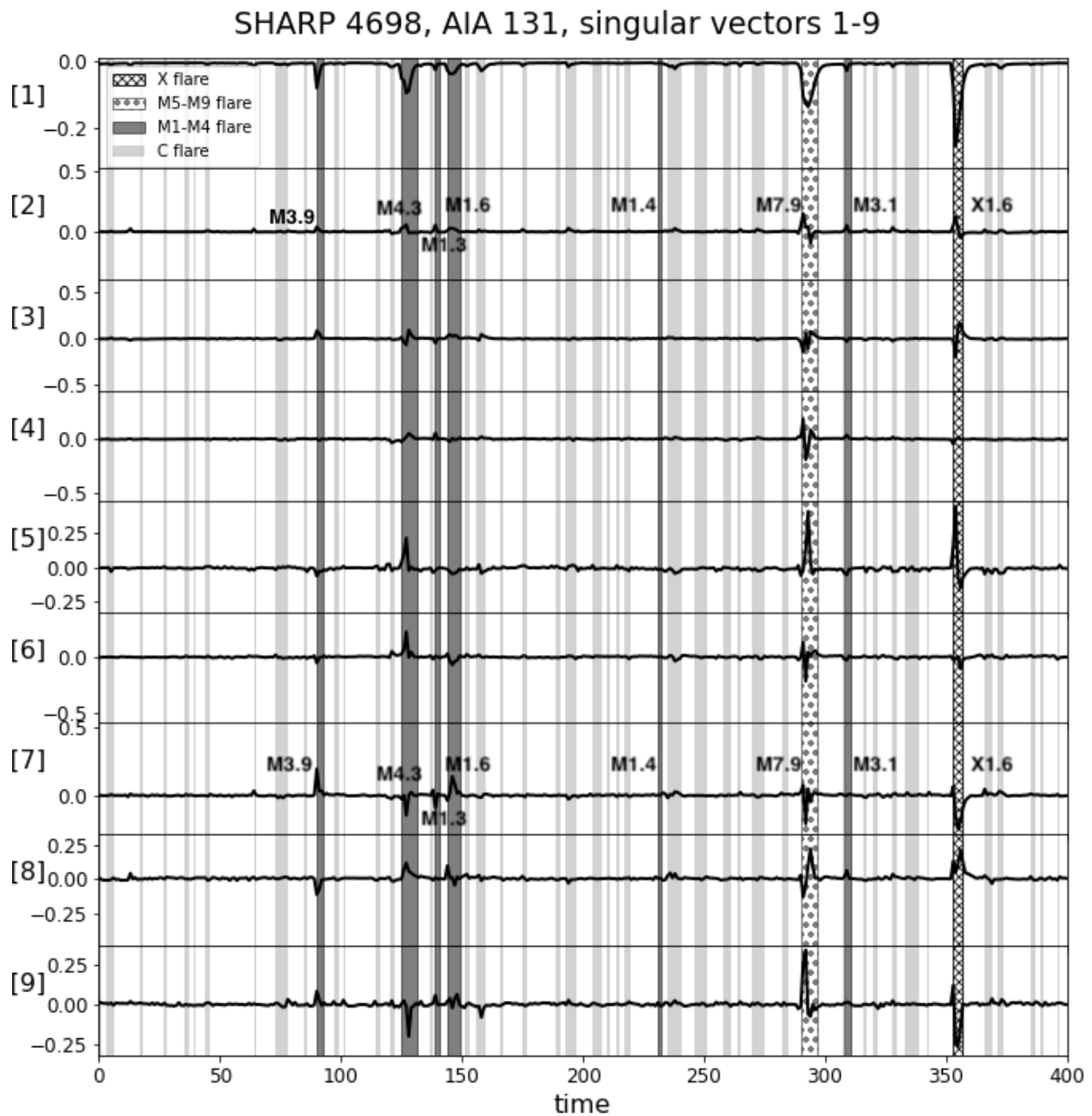
Figure 5.4: A plot of singular vectors 1-9 of the V matrix from taking the SVD of the summed SHARP matrix of SHARP 4698 in AIA 131 Å. The first 80 hrs of data for the SHARP are shown, with every 10 time steps on the x-axis representing 2 hrs.
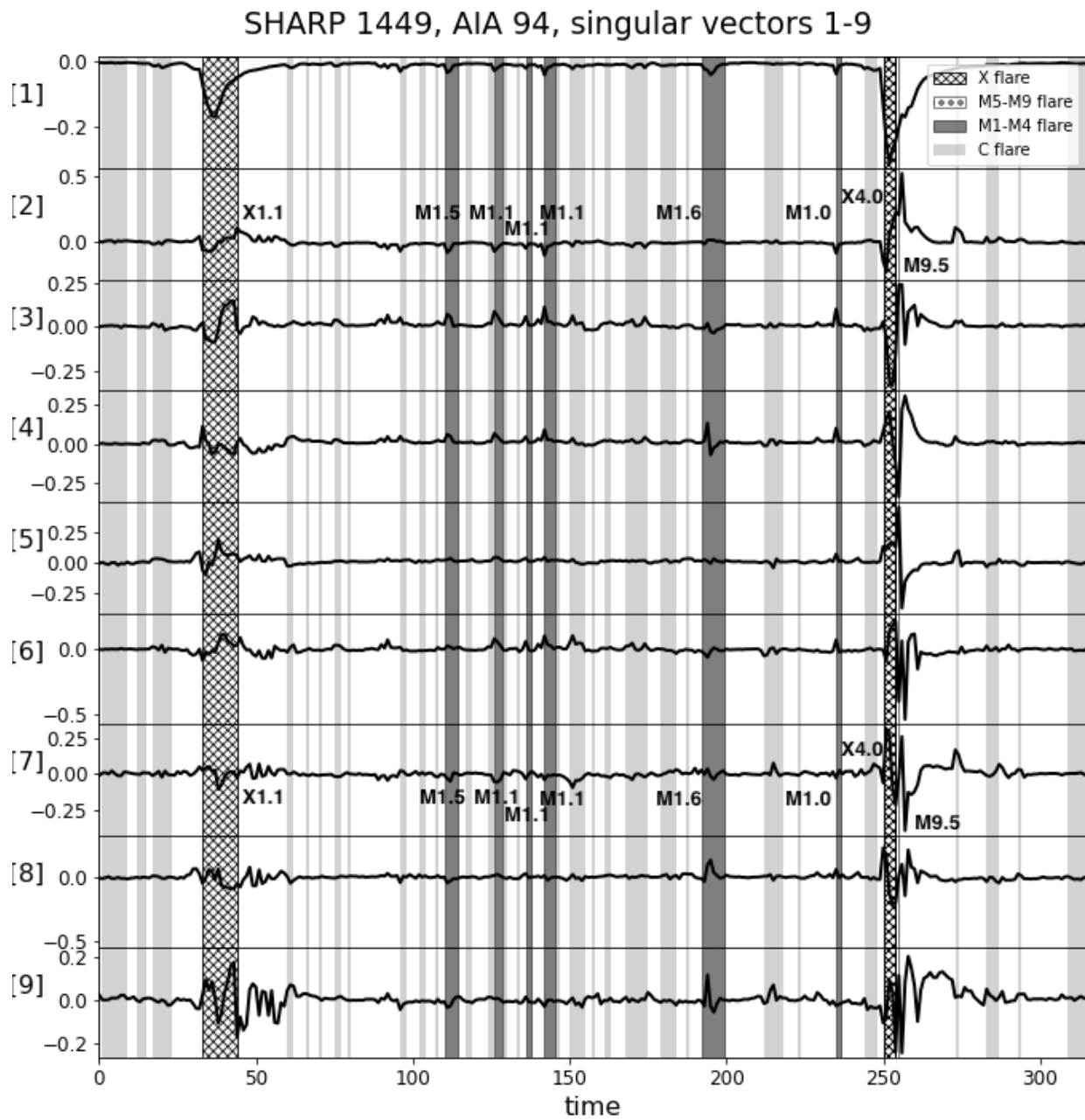
Figure 5.5: A plot of singular vectors 1-9 of the V matrix from taking the SVD of the summed SHARP matrix of SHARP 1449 in AIA 94 Å. The first 60 hrs of data for the SHARP are shown, with every 10 time steps on the x-axis representing 2 hrs.

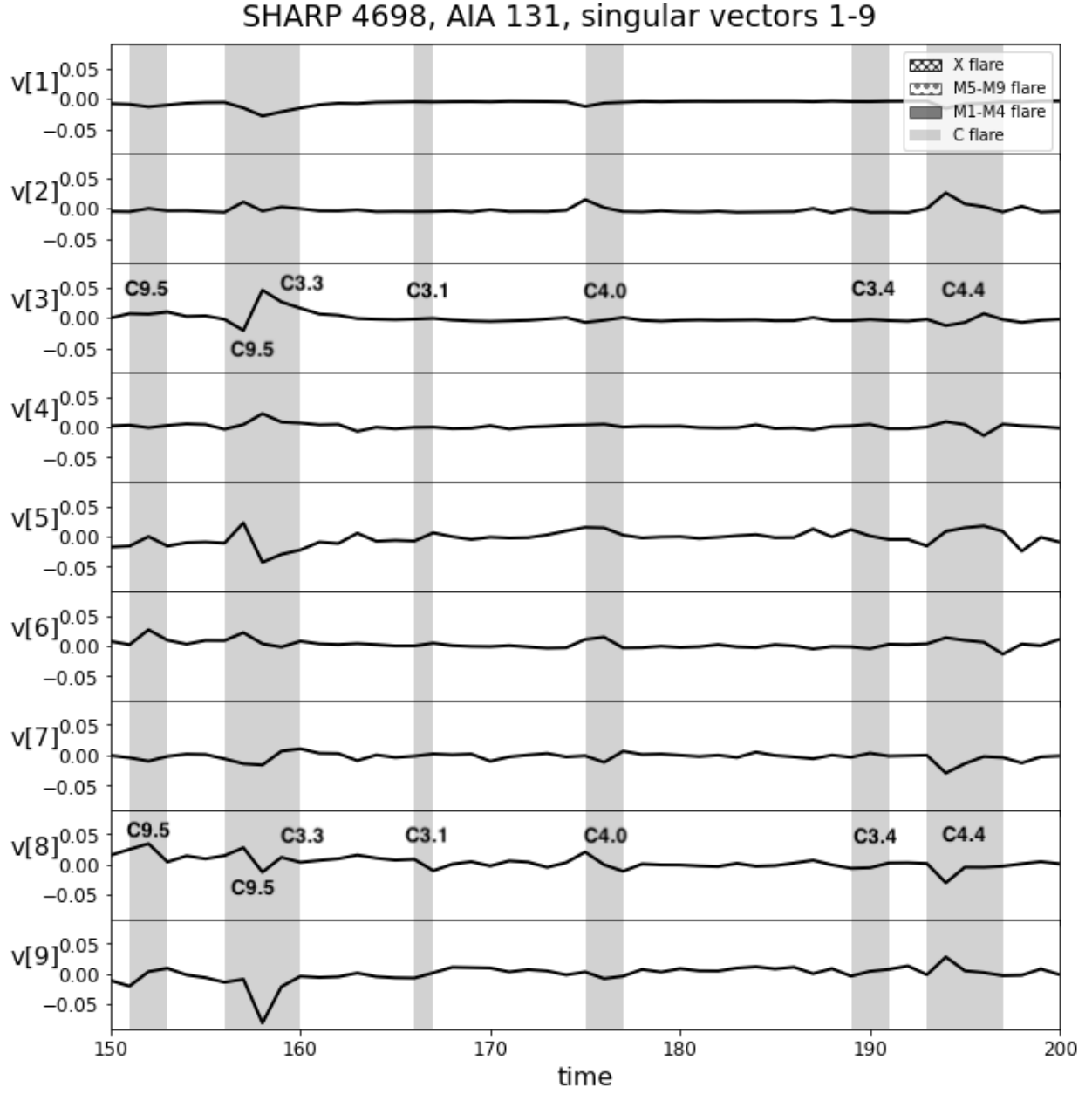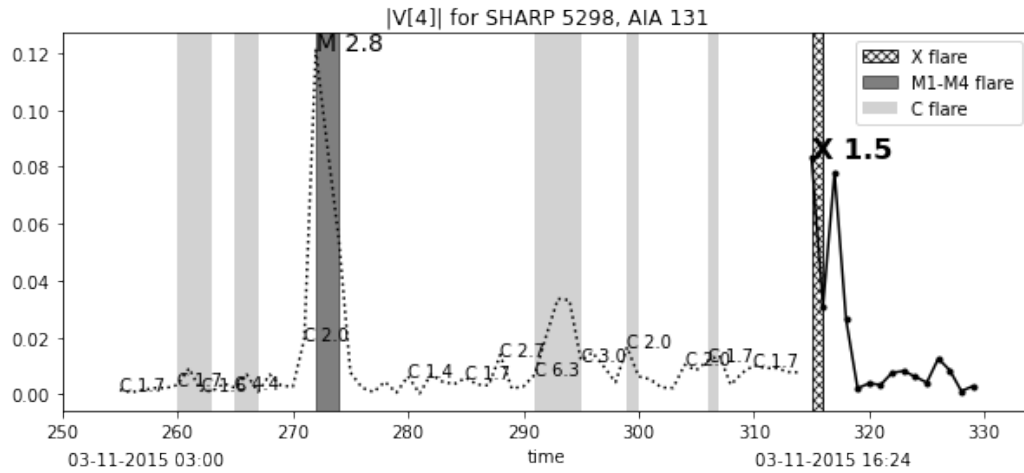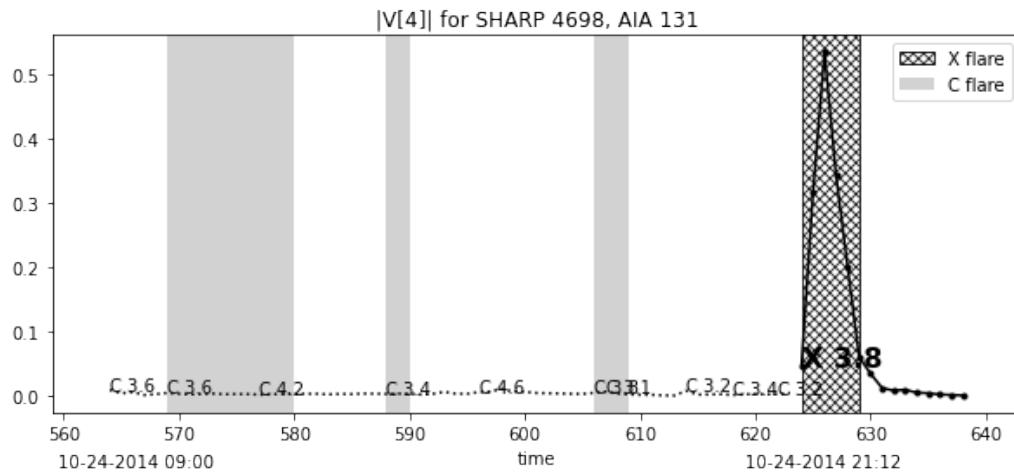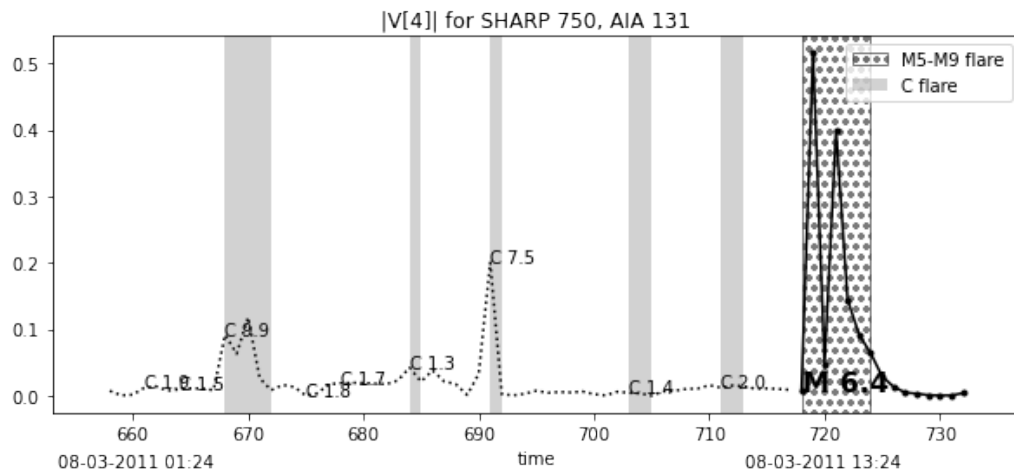Figure 5.6: A plot of singular vectors 1-9 of the V matrix from taking the SVD of the summed SHARP matrix for SHARP 4698 in AIA 131 Å. The singular vectors are cropped to show the 150-200th time steps, which represents 10 hrs.
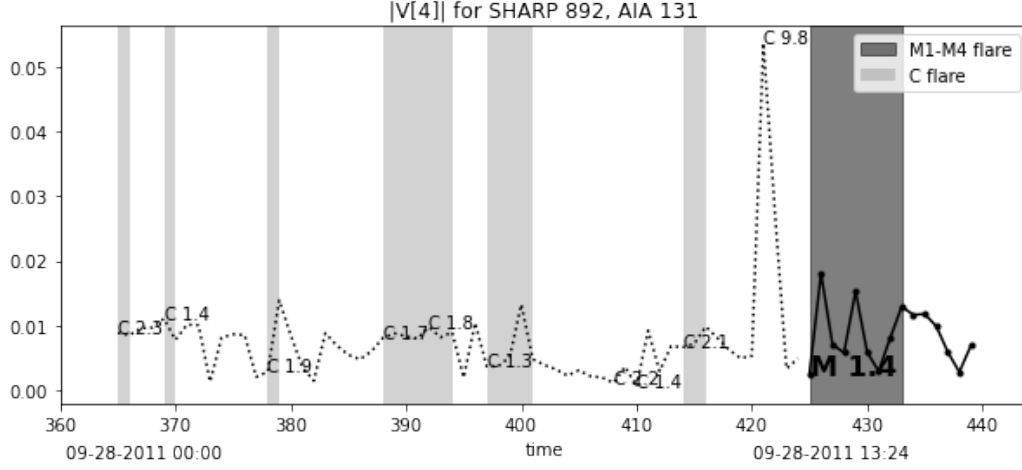
(a) A 12 hr sample preceding an X1.5 flare in SHARP 5298.

(b) A 12 hr sample preceding an X3.8 flare in SHARP 4698.

(c) A 12 hr sample preceding an M6.4 flare in SHARP 750.

(d) A 12 hr sample preceding an M1.4 flare in SHARP 892.

Figure 5.7: Examples of singular vector 4 samples (in absolute value) 12 hrs before a solar flare of interest. The 12 hr samples are represented by the dashed line, while the flare is represented by the solid line. Note that the y-axis varies across the plots for each SHARP.

singular vector 1 of the U matrix, u_1, we observe that the amplitude is very smooth and flat (see Figure 4.6 for an example). Since the amplitude of singular vector 1 of the V matrix, v_1, represents the amount of u_1 present at a given point in time (scaled by σ_1), the singular vector v_1 can be interpreted as containing information about the averaged pixel values of the AIA image data. Fine structure within the signals tends to appear in singular vectors 4-9. Drawing parallels with taking a Fourier transform of data, each successive singular vector resolves increasingly finer structure in the data until it eventually becomes physically irrelevant. With our data, this appears to be the case beyond singular vector 9, which is also shown by the decaying magnitude of the singular values in Figure 4.5. Table 5.1 describes in further detail the components of the data that can be observed by each singular vector.

Looking at the first 9 singular vectors, it was of interest to determine if any separation between flare classes (X, M5-M9, and M1-M4) could be seen within the samples. After separating the samples by flare class, we took the 25th and 75th percentiles of the amplitude over all the samples in a flare class at each timestep (Figure 5.8). For each flare class, we know that 50% of the precursor signal values lie between the plotted lines. The 25th percentile of all of the singular

vector amplitudes at each timestep remain fairly constant, representing a noise floor of the signal. In singular vector 1, we see that there are many more peaks in the 75th percentile line for the M5-M9 signal (Figure 5.8a). This suggests that there may exist a pattern of precursor flares occurring at the timesteps corresponding to those peaks in the M5-M9 signals. The sample amplitudes for the different flare classes had the greatest separation in singular vector 4, with both the M5-M9 and M1-M4 75th percentile lines noticeably higher than the X flare 75th percentile (Figure 5.8b). From the plot of singular vector 7 in Figure 5.8c, notice that the X flare 75th percentile line dips significantly below the others from about timestep 22 - 38 (which corresponds with approximately 4-8 hrs before a flare). There is potentially a dip in activity 4-8 hrs before an X-flare. The minimal activity between timesteps 22-38 can also be seen looking at the singular vector plots for the first 20 samples in Figure 5.9. In general, there is evidence in support of the fact that X flare precursor signals contain less activity than signals preceding M flares in the 12 hrs prior.

While it is convenient to divide flares into classes C, M, X, their magnitudes are continuous measurements. The flare class boundaries are rather arbitrary and present a challenge for characterizing properties of each flare class. For example, in flare prediction a M9.8 flare may have very similar properties to an X1.5 flare (and different properties than a low M flare), while a model is expected to classify the M9.8 flare and the X1.5 flare into different categories. Using this method of decomposing AIA image data, a peak for a C9.8 flare can appear much larger than an M1.4 flare as shown in Figure 5.7d. Depending on the singular vector chosen, the relative size of the smaller flare to the larger flare varies as well. Because it is difficult to distinguish flares solely by peak flux, it is necessary to identify unique patterns in precursor information that could give clues to the magnitude of an impending flare. These patterns could potentially be used as input features into flare prediction models in the future. We identify some properties of each of the flare classes identified with this SVD-based method.

In singular vector 1, the signal peak height and flare magnitude have a positive correlation (Example in Figure 5.4). Because the flare peaks align with the AIA catalog in time and the peak heights align with flare magnitudes in singular vector 1, we can use the peak heights in singular
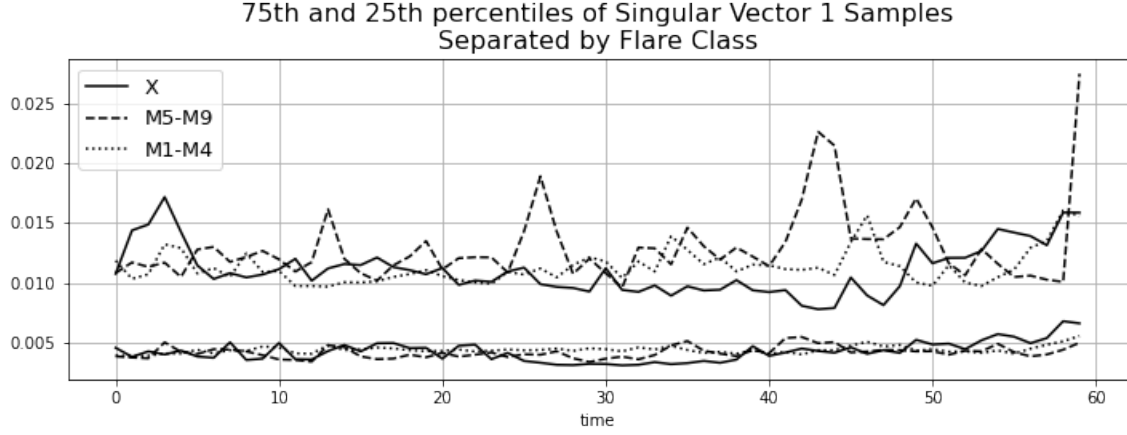
(a) The 75th and 25th percentiles of sample amplitudes in singular vector 1 for each flare class.
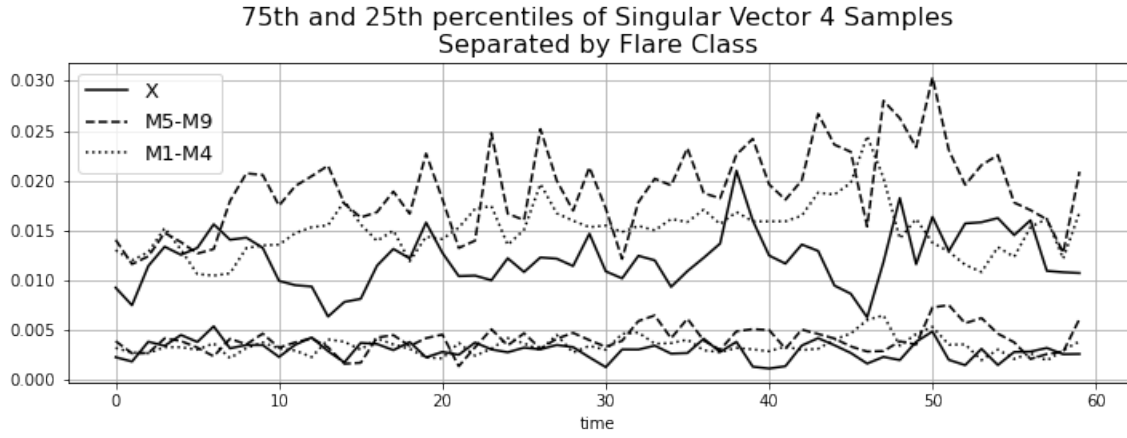
(b) The 75th and 25th percentiles of sample amplitudes in singular vector 4 for each flare class.
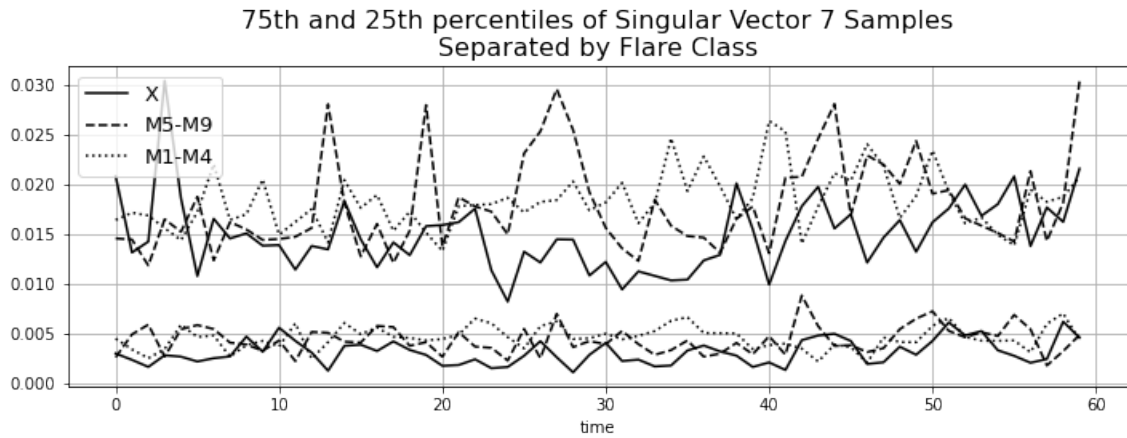
(c) The 75th and 25th percentiles of sample amplitudes in singular vector 1 for each flare class.

Figure 5.8: Plots of the 75th and 25th percentiles of sample amplitudes split by flare class.

Figure 5.9: A plot of all of the 104 samples from singular vectors 1-9. Samples 1-20 are X flare precursor signals, samples 21-46 are M5-M9 flare precursor signals, and samples 47-104 are M1-M4 flare precursor signals.
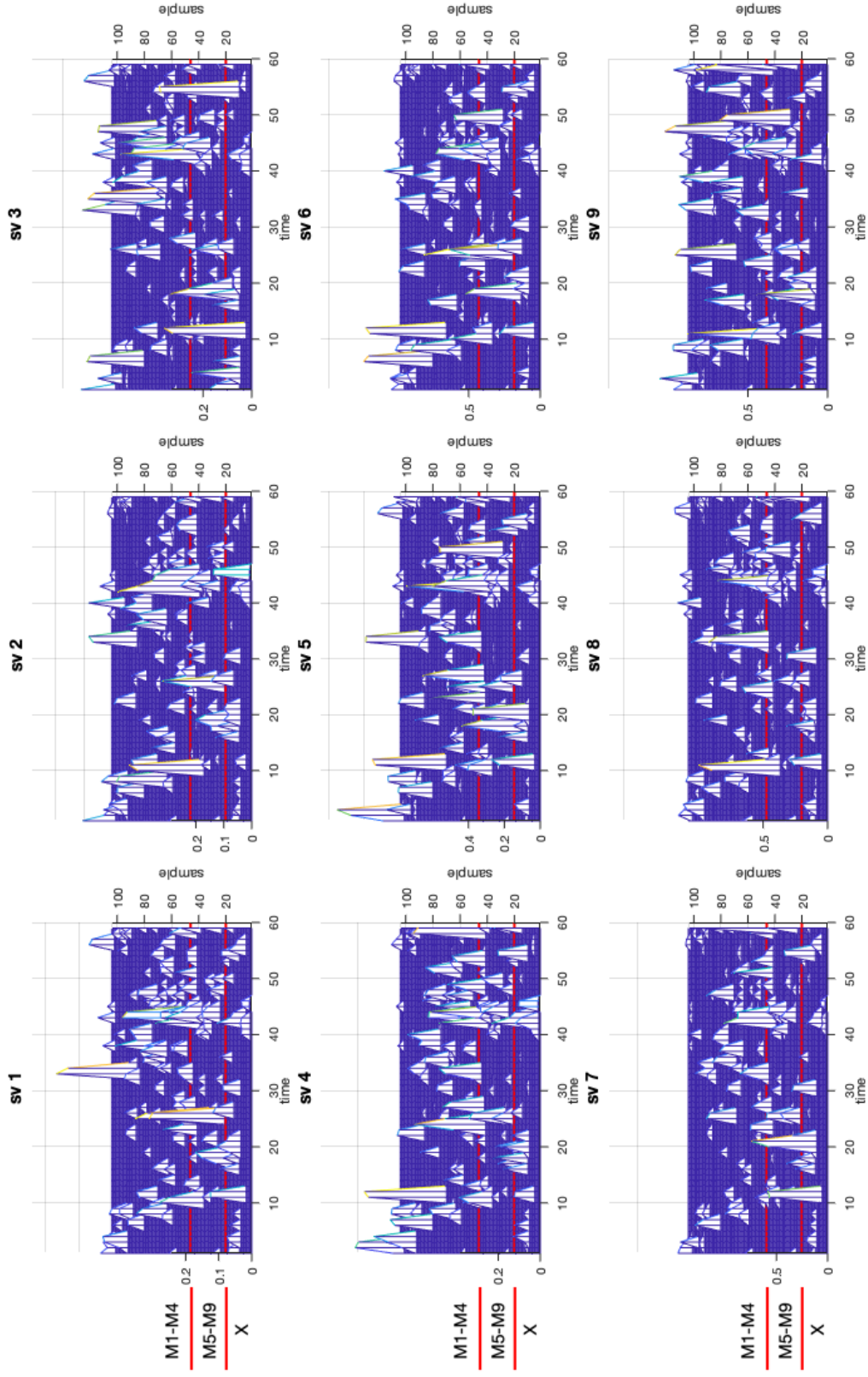
vector 1 to identify solar flares. Flare peaks that appear in singular value 1 also tend to appear as a peak in all subsequent singular vectors, often with smaller amplitude (Figure 5.9). In singular vectors 4-9, the relative peak amplitudes of the precursor flares tend to be much larger relative to the flare of interest. We analyze properties of the signals by flare class below:

X flares: We note that 5/20 of the X flares have an M1-M4 flare preceding them from the AIA catalog. Of these 5 instances, four of them occur between 8 and 10 hours before a flare. One of them occurs 11 hours before the flare. Over half (11/20) of the signals fall entirely below a threshold value of 0.2 (not scaled by the singular value) including the signals for the two X3 flares, suggesting there is not much precursor activity for many X flares. Compared to the maximum flare peak amplitude of approximately 0.7 in singular vector 4 for an X1.6 flare in SHARP 877, this provides further evidence that many X-flare precursor signals have little activity relative to M flares. Despite this, small spatial structure often appears in the 1-2 hours before an X flare in the higher singular vectors and the corresponding peaks become more well defined. Fourteen of the 20 X flares have a C flare in the 2 hours before the flare. As an example, we can see the precursor peaks become more defined in higher singular vectors for an X flare in SHARP 5298 in Figures 5.10 and 5.7a.

M5 - M9 Flares: Out of the 26 total M5-M9 flares, 8 of them have an M1-M4 flare preceding them. All but one of these peaks corresponds with a signal amplitude greater than 0.1 in singular vector 4. Of these 8 instances, 4 of them occur between 7-9 hours before a flare. 3 of them occur approximately 4 hours before a flare. One of them occurs approximately 10 hours before a flare. So approximately 30% of the M5-M9 flares are preceded by a precursor flare of magnitude M1-M4, and approximately 25% of the X flares are preceded by a M1-M4 precursor flare.

M1-M4 Flares: In total, we have 104 samples for the 12 hours before M1-M4 flares. There are 4-5 times more flares of this magnitude compared to X and M5-M9 flares. Of the 104 samples, only nine of them contain M1-M4 flares within the precursor signal. Five of the nine M1-M4 precursor flares occur between 9-11 hours before another M1-M4 flare. When plotting the samples by flare class, there is much more precursor activity in the flares with lower magnitude, especially
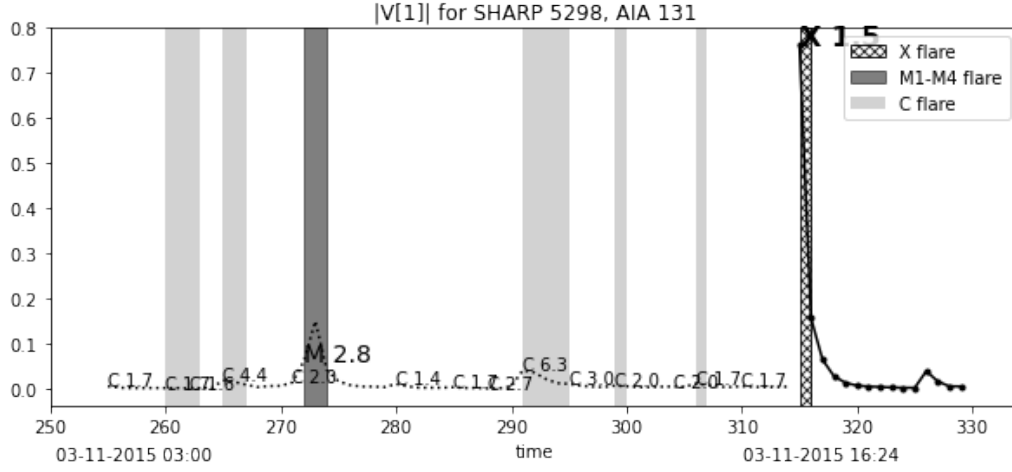
(a) A 12 hr sample in singular vector 1 preceding an X1.5 flare.
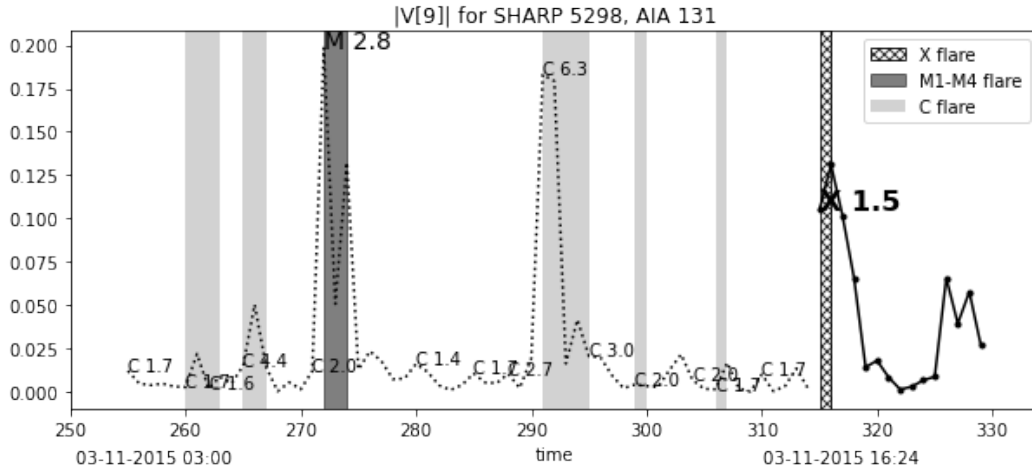
(b) A 12 hr sample in singular vector 9 preceding an X1.5 flare in SHARP 5298.

Figure 5.10: Examples of samples in different singular vectors for an X1.5 flare in SHARP 5298. Figure 5.7a shows the plot for the same flare in singular vector 4. The 12 hr samples are represented by the dashed line, while the flare is represented by the solid line.

in the higher singular vectors. In singular vector 8 for all of the X flares, a majority of the precursor signals have amplitudes below 0.2, while in the same singular vector for the M1-M4 flares, there is much more "popcorn"-like activity (Figure 5.11).

Because we have found that larger flares tend to have less precursor activity, we hypothesize that there is a period of time required for energy to build up in the solar atmosphere before a large flare is released.

Singular Vector 1 for Samples Preceding X flares

Singular Vector 8 for Samples Preceding X flares
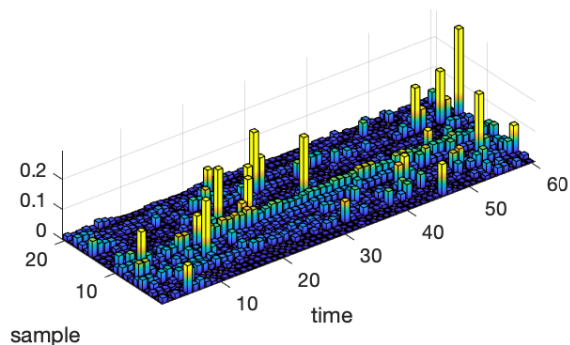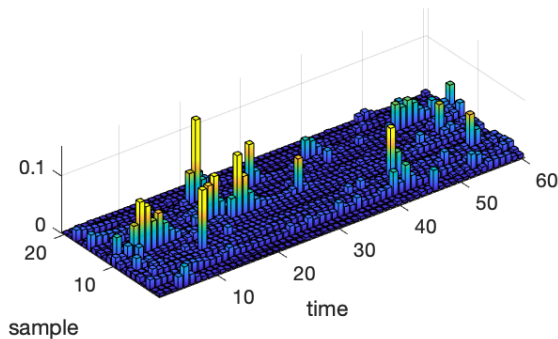
M5-M9 flares

M5-M9 flares
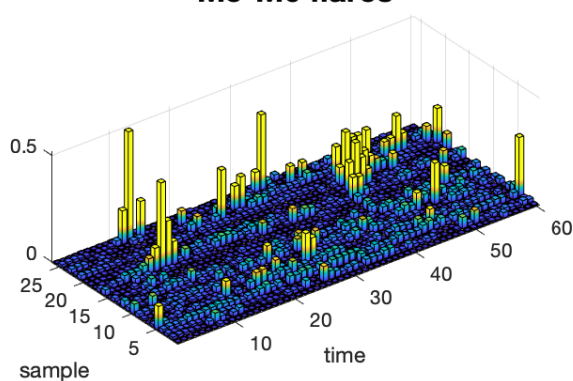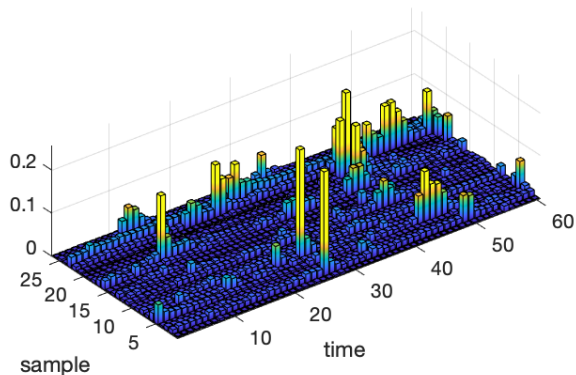
M1-M4 flares

M1-M4 flares

Figure 5.11: Bar plots of 12 hr samples by flare class.

Chapter 6

Conclusions and Future Work

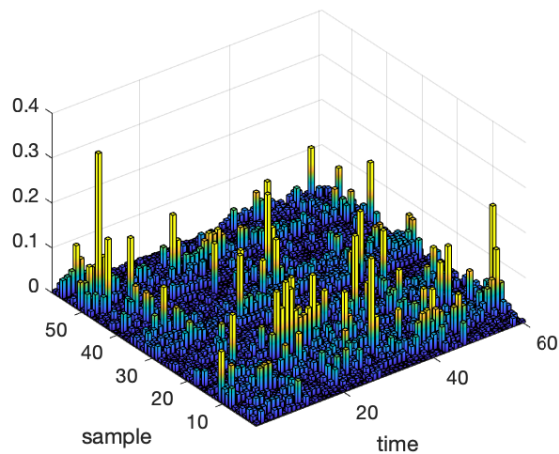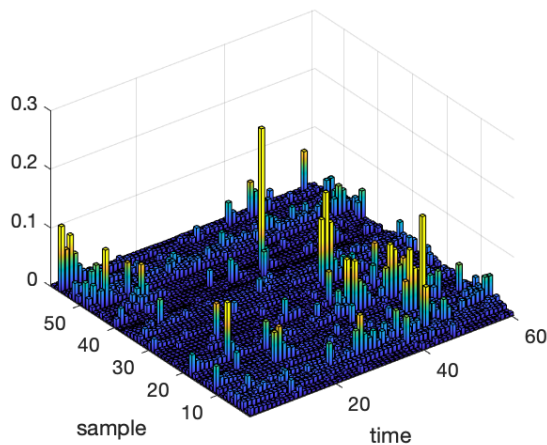In this work, we have presented an SVD-based method for identifying solar flare events with minimal loss of spatial information from a sequence of images. To illustrate the utility of this method, we performed an analysis of the time period leading up to large solar flare events to further understand the relationship between large solar flares and precursors. We showed that AIA active region images tend to be invariant to summing across rows or down columns, revealing that the spatiotemporal data has natural isotropic properties. Decomposing these summed matrices via SVD extracts the spatial and temporal modes and allows for the analysis of time series signals. Within the signals, peaks that distinguish flare classes align well with those given in the GOES X-ray Flare Catalog as used by SWPC and with newly created AIA flare catalog data. Finally, these resulting singular vector signals demonstrate there is less precursor activity in X flares compared to M flares.

There are many possible directions to take this work in the future. One of the major challenges with solar flare detection is simply the lack of events. We hope that further studies incorporate data from Solar Cycle 25. With more flaring samples, it could be possible to use machine learning techniques like neural networks and clustering to discover correlations in the precursor signals. Another obvious extension of this work would involve exploring different precursor activity windows. While we looked at a 12 hour time window before large solar flares, it would be useful to study time periods further back to elucidate patterns in precursor flare activity, especially as spatiotemporal data for each SHARP can span over a month. Finally, exploring this SVD-based method in the

context of rare event identification/prediction of other geophysical phenomena such as earthquakes, volcanic eruptions, or flooding, might reveal insights into precursors for these events as well.

Bibliography

[1] A profile of space weather. Technical report, NOAA Space Weather Prediction Center.

[2] K. Akabane. Some features of solar radio bursts at around 3000 Mc/s. Publications of the Astronomical Society of Japan, 8:173, January 1956.

[3] Jonathan Arad, Mashor Housh, Lina Perelman, and Avi Ostfeld. A dynamic thresholds scheme for contaminant event detection in water distribution systems. Water Research, 47(5):1899–1908, 2013.

[4] Markus J. Aschwanden and Samuel L. Freeland. Automated solar flare statistics in soft x-rays over 37 years of goes observations: The invariance of self-organized criticality during three solar cycles. The Astrophysical Journal, 754(2):112, July 2012.

[5] B. Bach, P. Dragicevic, D. Archambault, C. Hurter, and S. Carpendale. A descriptive framework for temporal data visualizations based on generalized space-time cubes. Computer Graphics Forum, 36(6):36–61, 2017.

[6] G. Barnes, K. D. Leka, C. J. Schrijver, T. Colak, R. Qahwaji, O. W. Ashamari, Y. Yuan, J. Zhang, R. T. J. McAteer, D. S. Bloomfield, P. A. Higgins, P. T. Gallagher, D. A. Falconer, M. K. Georgoulis, M. S. Wheatland, C. Balch, T. Dunn, and E. L. Wagner. A comparison of flare forecasting methods, I: Results from the "All-Clear" workshop. The Astrophysical Journal, 829(2):89, September 2016.

[7] G. Barnes, K. D. Leka, E. A. Schumer, and D. J. Della-Rose. Probabilistic forecasting of solar flares from vector magnetogram data. Space Weather, 5(9), 2007.

[8] M. G. Bobra, X. Sun, J. T. Hoeksema, M. Turmon, Y. Liu, K. Hayashi, G. Barnes, and K. D. Leka. The Helioseismic and Magnetic Imager (HMI) Vector Magnetic Field Pipeline: SHARPs – Space-Weather HMI Active Region Patches. Solar Physics, 289(9):3549–3578, September 2014.

[9] Aidan Boyd, Kevin Bowyer, and Adam Czajka. Human-aided saliency maps improve generalization of deep learning. May 2021.

[10] Bruno Brentan, Pedro Rezende, Daniel Barros, Gustavo Meirelles, Edevar Luvizotto, and Joaquín Izquierdo. Cyber-attack detection in water distribution systems based on blind sources separation technique. Water, 13(6):795, March 2021.

[11] Frédéric Chazal and Bertrand Michel. An introduction to topological data analysis: Fundamental and practical aspects for data scientists. Frontiers in Artificial Intelligence, 4, September 2021.

[12] Yang Chen, Ward B. Manchester, Alfred O. Hero, Gabor Toth, Benoit DuFumier, Tian Zhou, Xiantong Wang, Haonan Zhu, Zeyu Sun, and Tamas I. Gombosi. Identifying solar flare precursors using time series of sdo/hmi images and sharp parameters. Space Weather, 17(10):1404–1426, 2019.

[13] Bahram Choubin, Moslem Borji, Amir Mosavi, Farzaneh Sajedi-Hosseini, Vijay P. Singh, and Shahaboddin Shamshirband. Snow avalanche hazard prediction using machine learning methods. Journal of Hydrology, 577:123929, 2019.

[14] Robert D. Cicerone, John E. Ebel, and James Britton. A systematic compilation of earthquake precursors. Tectonophysics, 476(3):371–396, 2009.

[15] Brian R. Dennis. Solar hard x-ray bursts. Solar Physics, 100(1-2):465–490, October 1985.

[16] Brian R. Dennis. Solar flare hard x-ray observations. Solar Physics, 118(1-2):49–94, 1988.

[17] Varad Deshmukh, Thomas E. Berger, Elizabeth Bradley, and James D. Meiss. Leveraging the mathematics of shape for solar magnetic eruption prediction. J. Space Weather Space Clim., 10(13):16, April 2020.

[18] Shirley Dowdy, Stanley Wearden, and Daniel Chilko. Statistics for Research. Wiley, 2004.

[19] David Falconer, Abdulnasser F. Barghouty, Igor Khazanov, and Ron Moore. A tool for empirical forecasting of major flares, coronal mass ejections, and solar particle events from a proxy of active-region free magnetic energy. Space Weather, 9(4), 2011.

[20] David A. Falconer, Ronald L. Moore, Abdulnasser F. Barghouty, and Igor Khazanov. Prior flaring as a complement to free magnetic energy for forecasting solar eruptions. The Astrophysical Journal, 757(1):32, September 2012.

[21] F. Fárník, H. S. Hudson, M. Karlický, and T. Kosugi. X-ray and radio observations of the activation stages of an X-class solar flare. Astronomy and Astrophysics, 399(3):1159–1166, February 2003.

[22] F. Fárník and S.K. Savy. Soft x-ray pre-flare emission studied in Yohkoh-SXT images. Solar Physics, 183(2):339–357, 1998.

[23] Gene H Golub and Christian Reinsch. Singular value decomposition and least squares solutions. Linear algebra, 2:134–151, 1971.

[24] N. Gyenge, I. Ballai, and T. Baranyi. Statistical study of spatio-temporal distribution of precursor solar flares associated with major flares. Monthly Notices of the Royal Astronomical Society, 459(4):3532–3539, April 2016.

[25] I. G. Hannah, H. S. Hudson, M. Battaglia, S. Christe, J. Kašparová, S. Krucker, M. R. Kundu, and A. Veronig. Microflares and the statistics of x-ray flares. Space Science Reviews, 159(1-4):263–300, July 2011.

[26] L. K. Harra, S. A. Matthews, and J. L. Culhane. Nonthermal velocity evolution in the precursor phase of a solar flare. The Astrophysical Journal, 549(2):L245–L248, March 2001.

[27] R.A. Harrison. Coronal transients and their relation to solar flares. Advances in Space Research, 11(1):25–36, 1991.

[28] Seth M. Hirsh, Bingni W. Brunton, and J. Nathan Kutz. Data-driven spatiotemporal modal decomposition for time frequency analysis. Applied and Computational Harmonic Analysis, 49(3):771–790, 2020.

[29] Yoshiaki Ida, Eisuke Fujita, and Takashi Hirose. Classification of volcano-seismic events using waveforms in the method of k-means clustering and dynamic time warping. Journal of Volcanology and Geothermal Research, 429:107616, 2022.

[30] Jo Ann Joselyn. The Human Impact of Solar Flares and Magnetic Storms, pages 67–72. American Geophysical Union (AGU), 1998.

[31] Y. Y. Kagan and L. Knopoff. Statistical short-term earthquake prediction. Science, 236(4808):1563–1567, 1987.

[32] Rudrika Kalsotra and Sakshi Arora. Background subtraction for moving object detection: explorations of recent developments and challenges. The Visual Computer, 38(12):4151–4178, December 2022.

[33] Anuj Karpatne, Imme Ebert-Uphoff, Sai Ravela, Hassan Ali Babaie, and Vipin Kumar. Machine learning for the geosciences: Challenges and opportunities. IEEE Transactions on Knowledge and Data Engineering, 31(8):1544–1554, 2019.

[34] Gurbax S. Lakhina and Bruce T. Tsurutani. Geomagnetic storms: historical perspective to modern view. Geoscience Letters, 3(1), February 2016.

[35] E. Lippiello, L. de Arcangelis, and C. Godano. Time-energy correlations in solar flare occurrence. Astronomy and Astrophysics, 511:L2, February 2010.

[36] Edward T. Lu and Russell J. Hamilton. Avalanches and the distribution of solar flares. The Astrophysical Journal, 380:L89, October 1991.

[37] Warner Marzocchi, Christopher Newhall, and Gordon Woo. The scientific management of volcanic crises. Journal of Volcanology and Geothermal Research, 247-248:181–189, 2012.

[38] G. Medioni, I. Cohen, F. Bremond, S. Hongeng, and R. Nevatia. Event detection and analysis from video streams. IEEE Transactions on Pattern Analysis and Machine Intelligence, 23(8):873–889, 2001.

[39] Varun Mithal, Guruprasad Nayak, Ankush Khandelwal, Vipin Kumar, Nikunj C. Oza, and Ramakrishna Nemani. Rapt: Rare class prediction in absence of true labels. IEEE Transactions on Knowledge and Data Engineering, 29(11):2484–2497, 2017.

[40] Amir Mosavi, Pinar Ozturk, and Kwok wing Chau. Flood prediction using machine learning models: Literature review. Water, 10(11):1536, October 2018.

[41] S. A. Murray, S. Bingham, M. Sharpe, and D. R. Jackson. Flare forecasting at the Met Office Space Weather Operations Centre. Space Weather, 15(4):577–588, 2017.

[42] Michael P. Poland and Kyle R. Anderson. Partly cloudy with a chance of lava flows: Forecasting volcanic eruptions in the Twenty-First Century. Journal of Geophysical Research: Solid Earth, 125(1), 2020.

[43] Samira Pouyanfar, Yudong Tao, Saad Sadiq, Haiman Tian, Yuexuan Tu, Tianyi Wang, Shu-Ching Chen, and Mei-Ling Shyu. Unconstrained flood event detection using adversarial data augmentation. In 2019 IEEE International Conference on Image Processing (ICIP), pages 155–159, 2019.

[44] Tsuneji Rikitake. Earthquake prediction. Earth-Science Reviews, 4:245–282, 1968.

[45] Jacopo Selva, Warner Marzocchi, Paolo Papale, and Laura Sandri. Operational eruption forecasting at high-risk volcanoes: the case of Campi Flegrei, Naples. Journal of Applied Volcanology, 1(1), December 2012.

[46] Hong-Yan Shen, Qin Li, Yue-Ying Yan, Xin-Xin Li, and Jing Zhao. Separation of diffracted waves via SVD filter. Petroleum Science, 17(5):1259–1271, July 2020.

[47] Kazunari Shibata and Tetsuya Magara. Solar flares: Magnetohydrodynamic processes. Living Reviews in Solar Physics, 8, 2011.

[48] Adam B. Smith. U.S. billion-dollar weather and climate disasters, 1980 - present (NCEI Accession 0209268), 2020.

[49] S. J. Tappin. Do all solar flares have x-ray precursors? Astronomy and Astrophysics Supplement Series, 87(2):277–302, February 1991.

[50] Seiya Uyeda. Current affairs in earthquake prediction in Japan. Journal of Asian Earth Sciences, 114:431–434, 2015. Earthquake Precursory Studies.

[51] Kiera van der Sande, Natasha Flyer, Thomas E. Berger, and Riana Gagnon. Solar flare catalog based on SDO/AIA EUV images: Composition and correlation with GOES/XRS x-ray flare magnitudes. Frontiers in Astronomy and Space Sciences, 9, November 2022.

[52] Haimin Wang, Chang Liu, Kwangsu Ahn, Yan Xu, Ju Jing, Na Deng, Nengyi Huang, Rui Liu, Kanya Kusano, Gregory D. Fleishman, Dale E. Gary, and Wenda Cao. High-resolution observations of flare precursors in the low solar atmosphere. Nature Astronomy, 1(5), March 2017.

[53] M. S. Wheatland. A Bayesian approach to solar flare prediction. The Astrophysical Journal, 609(2):1134–1139, July 2004.

[54] Magnus M. Woods, Alberto Sainz Dalda, and Bart De Pontieu. Unsupervised machine learning for the identification of preflare spectroscopic signatures. The Astrophysical Journal, 922(2):137, November 2021.

[55] Manzhu Yu, Myra Bambacus, Guido Cervone, Keith Clarke, Daniel Duffy, Qunying Huang, Jing Li, Wenwen Li, Zhenlong Li, Qian Liu, Bernd Resch, Jingchao Yang, and Chaowei Yang. Spatiotemporal event detection: a review. International Journal of Digital Earth, 13(12):1339–1365, March 2020.